Aerospace Science and Technology, Volume 119, December 2021, Article number 107125
DOI:10.1016/j.ast.2021.107125

Impact of Installation on a Civil Large Turbofan Exhaust System at idle descent Conditions

Anirudh Narayan Rao[a], Ioannis Goulos[a], David G. MacManus[a]

[a] *Propulsion Engineering Centre, School of Aerospace, Transport and Manufacturing, Cranfield University, Bedfordshire, MK43 0AL, United Kingdom*

Abstract

Recent trends in civil aero-engine design aim at lowering specific thrust and improving propulsive efficiency by increasing the bypass ratio and therefore, usually also the fan diameter. The integration of these larger diameter engines with the airframe is critical to exhaust performance, and it is important to include these effects in engine performance analysis. The discharge coefficient of the bypass and core nozzles of a high-bypass ratio aero-engine at idle descent conditions is investigated numerically for an aero-engine in isolation and installed on an airframe. The discharge coefficients influence the engine operating conditions and turbomachinery re-matching at these off-design conditions. The maximum difference in the bypass nozzle discharge coefficient between the installed and isolated aero-engine across the descent phase is $\simeq 1.6\%$. The differences in the core nozzle discharge coefficient between the installed and the reference isolated configuration are $\simeq 43\%$ and $\simeq -5.4\%$ at the start and the end of the descent phase, respectively. The nozzle discharge coefficients depend on flight Mach number, incidence angle, and the nozzle pressure ratios of the fan and core nozzles. Multiple competing flow mechanisms govern the static pressure on the core nozzle base, which influences the core nozzle discharge coefficient. A novel reduced-order model is developed to estimate the core nozzle discharge coefficient for the installed configuration in idle descent conditions. This approach is based on the effective nozzle pressure ratio and can be implemented in engine performance simulations.

Keywords: Nozzle performance, aircraft aerodynamics, installation effects

NOMENCLATURE

Roman Symbols

$\dot{m}$	Mass flow rate, $kg\ s^{-1}$
A	Area or the rolling ball area, m^2

b	Wing span, m
c	Chord length of the wing, m
C_d, C_v	Discharge coefficient and velocity coefficient of the exhaust nozzle
C_L	Lift coefficient
C_p^{mod}	Modified pressure coefficient $= \dfrac{p - p_\infty}{p_\infty}$
D_{fan}, D_{nac}	Fan diameter and maximum nacelle diameter, respectively, m
k	Turbulent kinetic energy, $m^2\ s^{-2}$
M, Re	Mach number and Reynolds number
N	Number of samples
p, T	Static pressure and temperature, respectively, Pa, K
P_o, T_o	Total/Stagnation pressure and temperature, respectively, Pa, K
R	Ideal gas constant, $R = 287.05 J\ kg^{-1}\ K^{-1}$
r	Pearson's correlation coefficient
R^2	Coefficient of determination
U	Velocity, $m\ s^{-1}$
x, y, z	Co-ordinate descriptors
y^+	Non-dimensional wall distance

Greek Symbols

α	Aircraft incidence angle, $^\circ$
γ	Ratio of specific heats
κ	Thermal conductivity, $W/m\ K$
λ	Ratio of total pressure to static pressure
ω	Specific dissipation rate, s^{-1}
ρ	Density, $kg\ m^{-3}$
σ	Standard deviation

Superscripts

$()^{Bypass}$	Refers to the bypass nozzle
$()^{Core}$	Refers to the core nozzle
$()^{ideal}$	Refers to isentropically fully-expanded flow conditions
$()^{Vent}$	Refers to the air-vent nozzle

Subscripts

$()_{1,2..}$	Indices
$()_\infty$	Refers to ambient or freestream conditions
$()_b$	Refers to the base of the nozzle exit
$()_e$	Effective, for the effective nozzle pressure ratios
$()_{hi}$	Refers to the intake highlight plane

$()_{min,max}$	Refers to the minimum and maximum values, respectively
$()_p$	Prescribed, for the imposed nozzle pressure ratios
$()_{ref,nom,crit,loc}$	Refers to the reference, nominal, critical and local values, respectively
$()_{ROM}$	Refers to the estimated value from the reduced-order model
$()_{throat}$	Refers to the nozzle throat
Acronyms	
BPR	Bypass Ratio
$CNPR$	Core Nozzle Pressure Ratio $= \dfrac{P_o^{Core}}{p_\infty}$
ER	Extraction ratio $= \dfrac{FNPR}{CNPR} = \dfrac{P_o^{Bypass}}{P_o^{Core}}$
$FNPR$	Fan Nozzle Pressure Ratio $= \dfrac{P_o^{Bypass}}{p_\infty}$
$MFCR$	Mass Flow Capture Ratio $= \dfrac{A_\infty}{A_{hi}}$
NPR	Nozzle Pressure Ratio
$VNPR$	Vent Nozzle Pressure Ratio $= \dfrac{P_o^{Vent}}{p_\infty}$
0D and 3D	Zero- and Three-Dimensional, respectively
AIAA	American Institute of Aeronautics and Astronautics
CDA	Continuous Descent Approach
CFD	Computational Fluid Dynamics
CRM	Common Research Model
DSFRN	Dual Separate Flow Reference Nozzle
GCI	Grid Convergence Index
HBR	High Bypass Ratio
iCST	Intuitive Class-Shape Transformation functions
NASA	National Aeronautics and Space Administration
RMS	Root Mean Square
ROM	Reduced-Order Model
SST	Shear Stress Transport
VHBR	Very High Bypass Ratio

1. Introduction

1.1. Background

In the last few years, continuous descent approaches (CDA) at idle thrust settings have been considered for abatement of noise levels around airports, fuel savings and lower emissions [1, 2, 3]. The idle conditions correspond to the lowest operable aero-thermodynamic conditions for an aero-engine at a given flight Mach number, where the engine produces minimum thrust [4, 5]. At these off-design conditions, the changes to the core mass flow are substantially greater, because of larger resistance to the flow through the engine core as compared to the bypass duct [6]. Performance analysis tools are typically used to estimate the core mass flow in the preliminary engine design stage. The uncertainty associated with these predictions is large at idle conditions as the characteristics are extrapolated from above-idle operating conditions [7, 8]. Thus, it is imperative to obtain good estimates of the core mass flow for an aero-engine across the aircraft descent phase.

Exhaust systems for aero-engines are designed to accelerate the combusted gases from the engine core and the bypass air efficiently to maximise the gross thrust [9]. The two non-dimensional metrics used to assess the performance of the nozzles are the discharge coefficient and the velocity coefficient [10]. These coefficients provide a measure of the exhaust system losses, as well as external flow suppression effects. The discharge coefficient accounts for the losses in the boundary layer along the nozzle walls, flow blockages, and any other losses in total pressure [11]. The velocity coefficient is a measure of the gross propulsive force to the ideal isentropically expanded flow, with the loss in thrust due to boundary layers, shear layer interactions, mixing losses, the formation of shocks from the under or over-expanded jets and the interaction of the shocks with the boundary layer. Another factor is the pylon blockage of the annular ducts, which is taken into consideration while sizing the nozzle throat and exit areas. In the preliminary stages of engine design, the design optimisation of the nozzle aero-lines is carried out with respect to these two metrics [12]. However, external flow suppression effects, engine-airframe interaction, incidence effects, together with the engine cycle conditions, such as the nozzle pressure ratios of the bypass and the core nozzle play a significant role in determining the value of these performance metrics [13].

The last few decades have seen a gradual reduction in the specific thrust and an increase in the propulsive efficiency by increasing the bypass ratio (BPR) of a turbofan engine [14]. These consequently lead to an increase in the fan diameter (D_{fan}) and the overall engine size [15, 16]. Contemporary aero-engines typically operate at $BPR \simeq 9-12$ [17, 18, 19], and the engine integration with the airframe (or installation) becomes a highly significant factor in the overall aircraft's performance. The close-coupling of these engines with the wing could lead to higher interference drag [20, 21, 22, 23], and negate the gains of higher propulsive efficiency of the larger diameter engines [24]. For instance, the amount of lift loss by the inclusion of the nacelle and pylon on to an airframe was estimated to be around 10% for an under-wing podded engine [25]. The installation position, and in particular, the overlap of the wing and the nacelle influences the pressure field on the nacelle after-body and the exhaust system [13, 26], and this influences the discharge coefficient of the exhaust nozzles for both high bypass ratio (HBR) and very high bypass ratio (VHBR) engines. Thus, the wing-pylon-nacelle geometry design optimisation is required to minimise the interference drag between these parts [21, 27, 28, 29, 30, 31, 32]. It may be noted that structural, acoustic and safety considerations are also taken into account during the integration of aero-engines along with the aerodynamics considerations [33, 34].

Oliveira *et al.* [30] detailed the various aerodynamic interactions that need to be considered for the integration of an under-wing podded engine on to an airframe. The critical parameters to minimise the adverse effects of engine installation are the location along the wingspan, the overlap of the engine and the wing, and the pitch and toe angles of the engine. In-flight, several aerodynamic effects need to be accounted for, such as the formation of a "gully" between the wing, pylon and exhaust after-body which increases the local flow acceleration [30]. Furthermore, the interaction between the engine, wing and the airframe leads to flow acceleration and a reduction in the static pressure on the inboard side of the nacelle [35]. These aerodynamic effects have an impact on the exhaust nozzle performance and affect the net thrust produced by the engine and the mass flow from bypass and core nozzles.

For an aero-engine installed on an airframe, Otter *et al.* [13] showed that the performance metrics are affected by the axial and vertical location of the engine relative to the wing leading edge. Across the engine positions investigated at mid-cruise conditions, a variation of $\simeq 0.01\%$ in the bypass nozzle discharge coefficient, $\simeq 10\%$ in the core nozzle discharge coefficient and $\simeq 1\%$ in the velocity coefficient was observed for an installed engine compared to the isolated engine. Furthermore, for a change in the aircraft incidence angle of 4°, the variation in the core nozzle discharge coefficient was up to $\simeq 12\%$ for a fixed engine position. The large changes brought about by the installation affect the core mass flow, the operating point of the low-pressure turbine (LPT), and subsequently results in the fan operating at an off-design condition. The core nozzle discharge is further governed by the characteristics of the bypass jet efflux, which results in higher static pressure on the core cowl after-body, and this leads to further suppression of the core mass flow [36]. The core nozzle discharges to a static pressure which is different from the ambient pressure, and an "effective" nozzle pressure ratio needs to be considered [37, 13]. The effective nozzle pressure ratio is based on the static pressure at the exit of the core nozzle and accounts for the various aerodynamic effects resulting from the installation and engine operating conditions.

While previous studies investigated the impact of aero-engine installation at mid-cruise conditions [13, 21, 22, 23, 26, 38], there is a dearth of literature on the impact of installation on the engine performance metrics during the descent phase. At engine idle conditions, the bypass ratio of the engine is very high [5, 6], with very low mass flow passing through the engine core. Recent aviation safety regulations require engine manufacturers to determine the altitude relight envelope for engine restart in emergency descent conditions [39]. In order to determine the performance at these off-design conditions, good estimates of the mass flow through the engine exhaust systems are required during the preliminary engine design stage. The focus of recent studies has primarily been to predict the mass flows and windmilling drag of the bypass flow stream [40], and to obtain the compressor characteristics [41, 7]. Accurate predictions of the core nozzle discharge coefficient are required, as it can cause the turbomachinery components to re-match, which can subsequently affect the shaft speeds. This study aims to understand the performance of the bypass and core nozzles at idle descent conditions and to quantify the impact of installation on these metrics at various stages of the descent profile.

1.2. Scope of the current study

This study investigates the impact of installation on the bypass and core nozzle discharge coefficient at idle descent conditions for a HBR engine. The three-dimensional (3D) computational fluid dynamics (CFD) approach and performance accounting framework developed by Goulos *et al.* [26] is used to assess the aerodynamic effects at three levels of aero-engine integration: an isolated aero-engine with and without a pylon, and an under-wing podded aero-engine mounted on an airframe, which is representative of a typical twin-engine wide-body civil transport airliner. These levels of integration are considered to estimate the impact of the constituent installation effects related to incidence, nozzle pressure ratios, pylon, and airframe-wing interactions.

Across the aircraft descent phase, the mass and momentum flux from the exhaust nozzles are governed by the operating conditions such as the bypass and core nozzle pressure ratios, flight Mach number, incidence angle and the installation of the aero-engine. These parameters dictate the static pressure distribution on the exhaust system, and thereby, the nozzle discharge coefficients [13]. A novel reduced-order model (ROM) to estimate the nozzle discharge coefficient of the core nozzle is developed based on the limited dataset by relating the effective pressure at the nozzle exit to the mass flow from the nozzle [37]. Such models can be used in zero-dimensional (0D) performance tools for rapid evaluation of the engine performance at idle descent conditions.

The prescribed fan nozzle pressure ratio ($FNPR_p = \dfrac{P_o^{Bypass}}{p_\infty}$) and the prescribed core nozzle pressure ratio ($CNPR_p = \dfrac{P_o^{Core}}{p_\infty}$) decrease with flight Mach number (M_∞) for an aero-engine during the descent phase of an aircraft (Fig. 1). The extraction ratio ($ER = \dfrac{FNPR_p}{CNPR_p}$) is defined as the ratio of the fan nozzle pressure ratio to the core nozzle pressure ratio monotonically decreases from the top of descent to the end of descent. The nominal operating conditions are labelled ($M_0 ... M_6$), and this convention is retained for the remainder of this study. M_0 corresponds to mid-cruise conditions, while M_1 corresponds to flight conditions at the top/start of descent, and M_6 corresponds to a point at the end of descent. The aircraft incidence angle (α) changes across the descent profile, with the highest incidence angle at the end of descent (M_6).

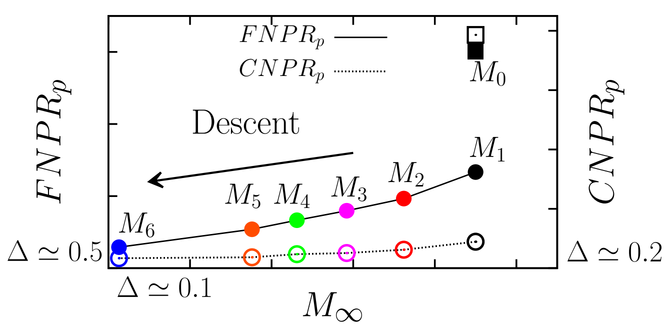

Figure 1: Variation of $FNPR_p$ (closed symbols) and $CNPR_p$ (open symbols) with flight Mach number. The mid-cruise condition (□, ■) is denoted by M_0, while the descent conditions (○, ●) are denoted by $M_1 - M_6$.

The article is organised as follows: Section 2 describes the methodology used to study the various configurations and compute the exhaust nozzle metrics. Section 3 details the effect of installation on the nozzle metrics and the sensitivities to changes in the incidence angle, fan and core nozzle pressure ratios on the metrics. A ROM to determine the core nozzle discharge coefficient for the installed aircraft is detailed in section 3.5, and this is followed by conclusions in section 4.

2. Methodology

The aerodynamic analysis for this study utilises the numerical framework developed for the design and analysis of separate-jet high and very high bypass ratio turbofan engines [10, 42, 12, 43, 44, 26]. In particular, the current study follows the methodology reported by Goulos *et al.* [26] for the design, meshing, CFD analysis, and performance evaluation of aero-engines [10, 45, 46]. Intuitive Class-Shape Transformation functions (iCSTs) were used for the design of the aerolines for the nozzles, pylon, intake, exhaust and the nacelle [47], in a similar manner as described in Goulos *et al.* [10, 48, 26]. The nacelle for the aero-engine was designed using the multi-objective method for 3D drooped and scarfed nacelles described by Tejero *et al.* [31, 49]. The aero-engine exhaust system consists of the bypass and core exhaust nozzle for the exit of the cooler bypass air, and the hot air gases from the engine core, respectively. The bypass nozzle is slightly convergent-divergent, and the core nozzle is convergent. The bypass nozzle is located upstream and above the core nozzle, and the inner duct wall of the bypass nozzle extends to form the core cowl after-body. An additional air-vent is situated on the core cowl after-body and is used to exhaust secondary airflows [43]. The inner duct wall of the core nozzle extends to form the conical core plug. The various components of the exhaust system are shown in Fig. 2(d).

2.1. Performance accounting

The performance of the exhaust focuses primarily on the nozzle discharge coefficients of the bypass and core nozzles. The discharge coefficient of a nozzle is defined as the ratio of the actual mass flow ($\dot{m}$) to the ideal mass flow under isentropic conditions at the nozzle throat area (A_{throat}). The rolling ball method is used for the computations of the nozzle throat areas [50]. The discharge coefficient is computed by:

$$C_d = \frac{\dot{m}}{\left(\frac{\dot{m}}{A}\right)_p^{ideal} A_{throat}} \tag{1}$$

The ideal mass flow is computed based on the total pressure (P_o) and total temperature (T_o) at the inlet of the nozzle. Here, the ideal gas constant is denoted by $R = 287.05 J\ kg^{-1}\ K^{-1}$. The ratio of specific heats is denoted by γ.

$$\left(\frac{\dot{m}}{A}\right)_p^{ideal} = P_o \left(\frac{1}{\lambda_p}\right)^{\frac{1}{\gamma}} \sqrt{\frac{2\gamma}{(\gamma-1)RT_o}\left(1-\left(\frac{1}{\lambda_p}\right)^{\frac{\gamma-1}{\gamma}}\right)} \tag{2}$$

λ_p denotes the prescribed nozzle pressure ratio (NPR_p), which is defined as the total pressure prescribed (or imposed) at the nozzle inlet (P_o) to the ambient static pressure (p_∞). The critical value of λ_p, $\lambda_{crit} = \left(\frac{\gamma+1}{2}\right)^{\frac{\gamma}{\gamma-1}}$ is used when $\lambda_p \geqslant \lambda_{crit}$. Across the idle descent range, this condition is not exceeded.

2.2. Engine and aircraft configurations

In order to systematically assess the impact of engine installation, three levels of integration of the aero-engine were considered: an isolated configuration without the pylon (Fig. 2(a)), an isolated engine with the pylon (Fig. 2(b)) and lastly, an installed configuration, where the aero-engine is mounted on an airframe in a conventional under-wing podded configuration (Fig. 2(c)). The airframe chosen for this study was the National Aeronautics and Space Administration (NASA) common research model (CRM) [51], which is typical of a twin-engine wide-body airframe with a seating capacity of approximately three hundred passengers [52]. A single installation position is considered for the under-wing podded configuration and is in line with contemporary HBR aero-engine positions (Fig. 2(e)). The aero-engine is pitched upwards by 1.75° and toed inwards by 2.25° with respect to the fuselage centreline, in accordance with the CRM "through-flow-nacelle" (TFN) [51]. For the isolated engines, the effective aerodynamic incidence angles were obtained by taking into account the pitch angle of the corresponding installed aero-engine on the airframe. In section 3.3, the sensitivity of the discharge coefficient to the incidence angle is assessed.

The sensitivity of the exhaust performance to the pylon top extension was investigated for a typical Very-High Bypass Ratio turbofan architecture. Two configurations were considered for the pylon top extension: a revolved pylon top and a pylon top-line filleting extension, where the edges of the flat top surface were filleted. The difference in C_d^{Bypass} between the revolved top (similar to the one investigated in the present study), and the filleted pylon top extensions was negligible, while the difference in C_d^{Core} was $< 1\%$ at mid-cruise conditions. Given the large variations in nozzle discharge coefficients across the idle descent conditions, the sensitivity of the pylon top extension methodology on the metrics is considered to be small for the isolated aero-engine investigated in this study.

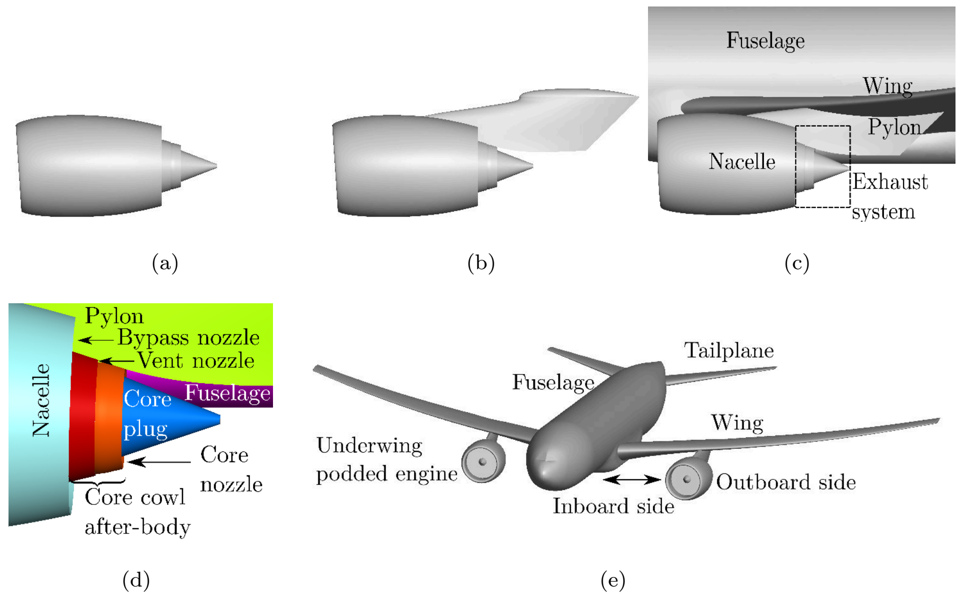

Figure 2: Image showing (a) isolated engine without the pylon, (b) isolated engine with the pylon, (c) under-wing installed engine viewed from the outboard side, (d) nomenclature of the exhaust system for the installed configuration, and (e) the under-wing podded aero-engine installed on the CRM airframe in perspective view.

2.3. CFD methodology

The half-models of the three configurations were placed in a hemispherical domain. The diameter of the hemispherical domain for the installed configuration was $\simeq 100c_{ref}$, where c_{ref} is the CRM wing reference chord length [51]. This is in accordance with the guidelines from the 4^{th} AIAA drag prediction workshop [53]. For the isolated configurations, the domain size was $\simeq 125D_{nac}$, where D_{nac} is the maximum nacelle diameter. The CFD approach including meshing and solution techniques established in Goulos *et al.* [26] for VHBR engine on the NASA CRM was used. A hybrid meshing strategy was employed, which consisted of near-wall prism layers to capture the boundary layers, and unstructured tetrahedral elements growing progressively from the prism layers to the boundaries of the domain [54]. The first cell height of the prism layers was placed to ensure $y^+ < 1$ for all viscous walls. Refinement regions consisting of unstructured elements were added in the vicinity of the critical areas such as the nozzle exits and the wing leading edges. The near-wall surface refinement was carried out based on the local wall-curvature and surface-proximity features [55]. The surface mesh on the fan face, intake and spinner is shown in Fig. 3(a), and the exhaust systems and the pylon is shown in Fig. 3(b).

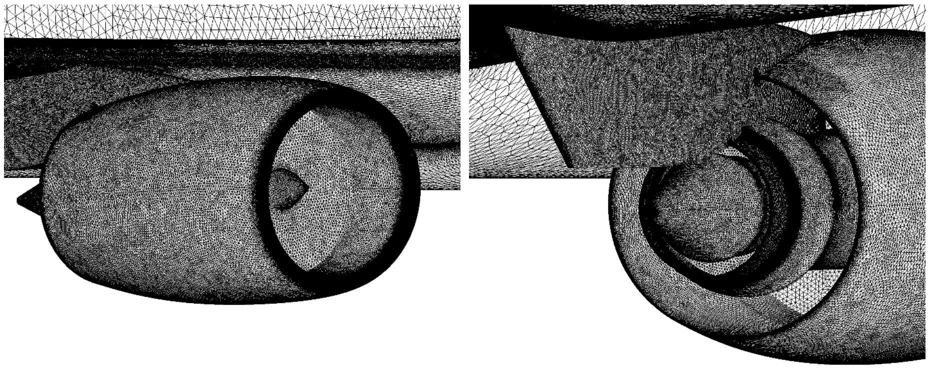

(a) (b)

Figure 3: Close-up of the surface mesh of the installed aero-engine showing (a) the fanface, intake spinner and the nacelle, and (b) the exhaust systems and the pylon in perspective view.

For the VHBR engine mounted on the NASA CRM [26], a grid independence analysis was carried out using meshes comprising of approximately 70×10^6, 130×10^6, and 288×10^6 elements [56]. The second-order grid convergence indices (GCI) for C_d^{Bypass} and C_d^{Core} corresponding to the 130×10^6 element mesh were found to be of the order of $\simeq 0.0015\%$ and $\simeq 0.23\%$, respectively. Meshes of similar spatial resolution were used for the CFD analysis here. For the installed configuration with the HBR engine considered in this study, the domain comprised of approximately 120×10^6 elements, and approximately 60×10^6 and 43×10^6 elements for the isolated configuration with and without the pylon, respectively.

An implicit density-based compressible solver with a second-order upwind spatial discretisation scheme with an implicit time integration formulation was used to solve the Favre-averaged Navier–Stokes equations [57]. The $k-\omega$ Shear Stress Transport (SST) model was implemented to close the turbulence equations [58]. The Green-Gauss node-based method was used for the calculation of the flow-field gradients. Thermal conductivity (κ) was computed according to the kinetic theory [59]. An 8^{th} order piecewise polynomial expression for the variable gas properties was employed for the calculation of specific heat capacity as a function of static temperature [5]. Sutherland's law was applied for the computation of dynamic viscosity [60].

The aero-thermal conditions at various points along the descent profile were obtained from an engine performance analysis tool, which provided the averaged total quantities (P_o, T_o) at nozzle inlets and the mass flows for the engine and the individual nozzles. The outputs from the performance analysis provided the input boundary conditions for the CFD analysis. A pressure far-field boundary condition taking into account the static temperature, pressure and the Mach number was imposed on the outer boundaries of the domain, and a symmetry boundary condition was used for the longitudinal plane which encloses the hemispherical domain. A pressure-inlet boundary condition was used to model the bypass, core and vent nozzle inlets, while a pressure-outlet boundary condition was used at the fan-face. The vent nozzle pressure ratio ($VNPR_p = \frac{P_o^{Vent}}{p_\infty}$) was set as a function of the prescribed fan nozzle pressure ratio over the idle descent range. The walls of the ducts, nacelle, pylon and the airframe were set as adiabatic and viscous no-slip walls. At the pressure-inlets, the total temperature and total pressure conditions were specified. A target mass flow was imposed at the fan-face boundary to ensure correct mass flow capture ratio ($MFCR$), which is defined as the ratio of the flow area of pre-entry streamtube at upstream infinity (A_∞) to the area of the intake highlight plane (A_{hi}). At subsonic mid-cruise conditions, $MFCR \simeq 0.7$ [11], while at windmilling and off-design conditions, $MFCR$ can be as low as 0.3 [36].

For the simulations performed here, the thermodynamic cycle re-matching of the engine was not performed, and the reported discharge coefficients were computed based on the mass flows through nozzles calculated based on CFD with prescribed and fixed values of $FNPR$ and $CNPR$. To ensure convergence of the metrics, the continuity and momentum residuals were reduced by four orders of magnitude. Additionally, the metrics of interest in this study, the reported discharge coefficients of the bypass (C_d^{Bypass}) and the core nozzles (C_d^{Core}) were based on the final value at the end of each simulation. The maximum variation from the final reported value was less than ± 0.0005 of the mean value computed over the last 200 iterations. The CFD methodology used in this study has previously been used in the design analysis of HBR and VHBR aero-engines [26, 38, 44, 12, 61].

2.4. Validation and verification of the CFD methodology

This study follows the CFD methodology and computation of the performance metrics presented by Goulos *et al.* [26]. The validation of the CFD methodology and the exhaust performance metrics were carried out for the NASA CRM and the Dual Separate Flow Reference Nozzle (DSFRN), respectively. The pertinent findings from the validation study of [26] are summarised here. For the NASA CRM, the CFD methodology was validated in terms of airframe and installation drag using experimental data [52]. Simulations were carried out for $M_\infty = 0.85$, $Re_{cref} = 5 \times 10^6$, where $Re_{c_{ref}}$, is the Reynolds number based on the reference wing chord (c_{ref}) for a lift coefficient of $C_L = 0.5$. Analyses were conducted for the "clean-wing", and the "through-flow-nacelle" (TFN) CRM configurations, to evaluate the installation drag. For the TFN CRM configuration, mesh independence was evaluated using meshes comprising of 14×10^6, 30×10^6, and 50×10^6 elements. For the "clean wing" CRM configuration, meshes with 7×10^6, 14×10^6, and 29×10^6 were used. For both configurations, the GCI was below 1% with regards to the medium mesh. The airframe drag coefficient was determined within approximately 13 drag counts of the measured data. The associated installation drag was calculated within two drag counts of the experimental measurements. These results are in agreement with those reported in the literature [62].

The validation of the exhaust performance using the DSFRN by Goulos *et al.* [26] is reported here. Analyses were performed for $1.4 \leqslant FNPR_p \leqslant 2.8$ at ground-level static conditions ($M_\infty \simeq 0$) for a constant $ER = 1.2$ [63]. A mesh independence analysis was carried out using 40 $\times10^6$, 80 $\times10^6$, and 120 $\times10^6$ elements. A difference in velocity coefficient (C_v) of 0.003% was found between the medium and fine meshes. The Root Mean Square (RMS) distance between CFD predictions and measured data, was found to be of the order of 0.04%, 0.30%, and 0.42% for C_v, C_d^{Bypass} and C_d^{Core}, respectively.

3. Results

3.1. Variation of the discharge coefficients at cruise conditions

The variation of the discharge coefficients of the bypass and core nozzles with their corresponding nozzle pressure ratios for the installed engine and the isolated engine with the pylon is investigated at a Mach number representative of the mid-cruise condition. For these cases, the extraction ratio and the incidence angle are held constant and, the values reported were obtained for the aircraft lift coefficient of 0.5. The bypass nozzle discharge coefficient asymptotes to a near-constant value on increasing $FNPR_p$ [46], which indicates that the bypass nozzle has choked (Fig. 4(a)). The impact of installation is discernible at the lowest $FNPR_p$, with the installed aero-engine having a marginally higher bypass nozzle discharge coefficient ($\simeq$ 0.4%) compared to the isolated case on account of the increased suction on the inboard side of the nacelle due to the engine-airframe interaction and the gully flow effect [37, 35]. At mid-cruise conditions, the bypass nozzle typically operates at choked conditions, and the mass flow from the bypass nozzle is insensitive to the impact of installation and external flow effects [37].

For the range of $FNPR_p$ considered, the extraction ratio is held constant, and thus, $CNPR_p$ increases monotonically with $FNPR_p$. A monotonic increase in

C_d^{Core} is observed for both the configurations with an increase in $CNPR_p$, until the core nozzle chokes at higher values of $CNPR_p$, and no further increase in C_d^{Core} is possible (Fig. 4(b)). At the lowest $CNPR_p$, C_d^{Core} for the isolated engine is $\simeq 16.3\%$ lower compared to its installed counterpart. The differences between the installed and the isolated engine C_d^{Core} values decrease as $CNPR_p$ is increased. At low $CNPR_p$, the freestream Mach number suppression effects are counteracted by the engine-airframe interaction effects on the inboard side for the installed case. This leads to an increase in C_d^{Core} for the installed configuration compared to the isolated configuration with the pylon. As expected, the discharge coefficient increases with NPR_p for the bypass and core nozzles, until λ_{crit} is reached. As the core nozzle operates at $\lambda_p \lesssim \lambda_{crit}$ at mid-cruise conditions, C_d^{Core} is sensitive to external flow effects. At mid-cruise conditions, the difference in C_d^{Core} between the installed and the isolated configuration is $\lesssim 1\%$.

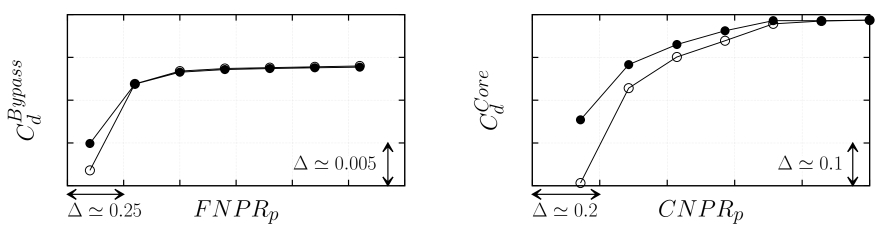

(a) (b)

Figure 4: Variation of (a) bypass nozzle discharge coefficient with fan nozzle pressure ratio, and (b) core nozzle discharge coefficient with core nozzle pressure ratio for the aero-engine installed on the airframe (●), and the isolated engine with the pylon (○) at mid-cruise conditions.

Results are presented using the contours of the modified pressure coefficient, $C_p^{mod} = \dfrac{p - p_\infty}{p_\infty}$ for the three levels of engine integration considered at mid-cruise condition, M_0 (Fig. 5). The contour levels of C_p^{mod} were chosen to accentuate the flow features and to highlight the differences between the installed and the isolated configurations at a given flight condition. The inclusion of the pylon on the isolated engine leads to the change in the static pressure distribution on the core cowl after-body and the core plug (dashed box in Fig. 5(b)), while larger changes are observed when the engine is mounted on to the airframe (Fig. 5(c) and Fig. 5(d)). On the inboard side of the installed engine (Fig. 5(c)), a reduction in the static pressure distribution is observed as compared to the outboard side (Fig. 5(d)) on account of the interaction between the engine and the fuselage, which leads to flow acceleration between the fuselage and the engine inboard side [35]. Lower values of C_p^{mod} are observed on the nacelle, core cowl after-body (dashed box in Fig. 5(c)), core plug, and the pylon on the inboard side compared to the outboard side of the installed engine and the isolated engine with the pylon.

On account of the swept wing of the aircraft, the aero-engine has a larger axial overlap of the wing on the inboard side as compared to the outboard side, which results in differences in the flow topology on either side. The effective flow area between the engine and the airframe is reduced due to the proximity of the nacelle, pylon and wing, which results in flow acceleration and the formation of shocks on the core cowl after-body and the core plug. Lower values of C_p^{mod} are observed on the pylon-wing junction on the inboard side (Fig. 5(c)) on account of the "gully flow" effect [30, 26]. This is due to flow over-acceleration, which terminates with a strong normal shock on the inboard side of the pylon (above the dashed box in Fig. 5(c)). On the outboard side of the installed engine, the signature of the shocks on the pylon surface (dashed box in Fig. 5(d)) has a pattern similar to that observed for the isolated engine at the corresponding location (Fig. 5(b)). Thus, the engine-airframe interaction leads to a reduction in the static pressure on the inboard side as compared to the outboard side.

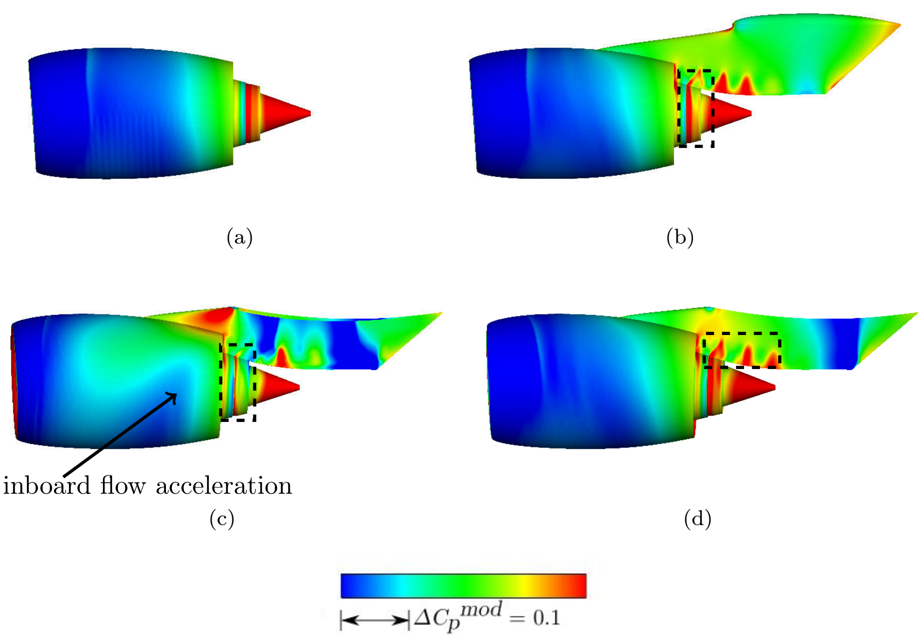

Figure 5: Contours of C_p^{mod} at the mid-cruise condition (M_0) for (a) isolated aero-engine without the pylon, (b) isolated aero-engine with the pylon, (c) inboard side of the installed aero-engine, and (d) outboard side of the installed aero-engine. Flow is from left to right in these images.

Therefore, a combination of flow mechanisms leads to differences between the discharge coefficients of installed and the isolated configurations at mid-cruise conditions, and affect the static pressure in the vicinity of the nozzle exits. The differences are larger when the nozzle pressure ratio is below λ_{crit}.

3.2. Variation of the discharge coefficient across the descent profile

The variation of the discharge coefficients at specific points along the descent profile is investigated for the various levels of integration. The fan and core nozzle pressure ratio decreases with altitude and flight Mach number along the descent profile (Fig. 1). For the installed configuration, the aircraft's wing pressure field influences the nozzle metrics [13]. At cruise conditions, the lift coefficient (C_L) of the "clean-wing" CRM aircraft was approximately 0.5. For descent conditions $M_1 - M_5$, the lift coefficient of the aircraft in the installed configuration was approximately 0.3, and at the end of descent at M_6, the lift coefficient was approximately 0.5. The non-dimensional lift coefficient ($C_{L,loc}\ c_{loc}/c_{ref}$) along the wingspan varies marginally between M_1 and M_5, and at M_6, the local lift coefficient is higher compared to the other cases on account of the increased aircraft incidence at the end of descent (Fig. 6). Here, $C_{L,loc}$ is the local lift coefficient obtained at the wing cross-section of chord length c_{loc}.

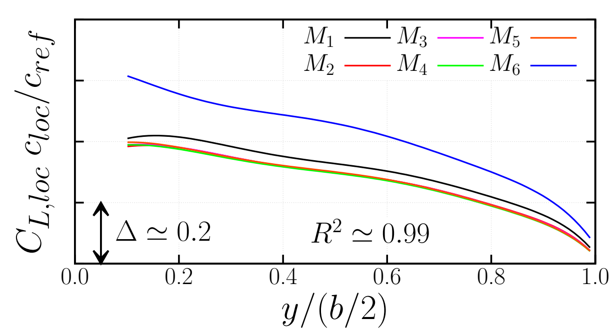

Figure 6: Curves of best fit showing the variation of the non-dimensional lift coefficient ($C_{L,loc}\ c_{loc}/c_{ref}$) along the wingspan at idle descent conditions. Here, $y/(b/2) = 0$ corresponds to the wing root and $y/(b/2) = 1$ corresponds to the wing tip. Note that for flight conditions M_2 to M_5, the curves overlap.

The discharge coefficient of the bypass nozzle for the installed aero-engine varies by $\simeq 3\%$ across the idle descent range (Fig. 7(a)). C_d^{Bypass} decreases monotonically by $\simeq 1.2\%$ between the top of descent (M_1) and a condition close to the end of descent (M_5). The impact of the engine-airframe interaction decreases with descent progression, as does the $FNPR_p$, which leads to a decrease in C_d^{Bypass}. At the final descent point M_6, a further reduction in C_d^{Bypass} of $\simeq 1.8\%$ is observed compared to M_5. The incidence angle of the aircraft is higher at the end of descent at M_6 by about $\Delta\alpha = 2° - 2.5°$ compared to the other operating points. The increased incidence results in a higher static pressure field due to the wing loading, and acts on the exhaust system for the installed configuration, which leads to a decrease in the discharge coefficients [13]. The variation in C_d^{Bypass} across the descent profile is $\lesssim 1\%$ for both configurations of the isolated engines.

The discharge coefficient of the core nozzle for the installed aero-engine shows a variation of $\simeq 8.3\%$ as the aircraft descends (Fig. 7(b)), due to the reduction in $CNPR_p$ and the engine-airframe interaction from the top of descent (M_1) to the end of descent (M_6). At the top of descent (M_1), the installed engine has $\simeq 43\%$ higher C_d^{Core} values compared to the corresponding isolated engine with the pylon. At a flight condition close to the end of descent (M_5), this difference decreases to $\simeq 18.4\%$, which indicates that the impact of installation on C_d^{Core} is significant for a large part of the descent phase. However, at the lowest flight Mach number (M_6), the difference in C_d^{Core} between the installed and isolated engine with the pylon is $\simeq -5.4\%$. On account of the higher incidence angle for the installed case at the end of descent (M_6), the increased wing loading suppresses the core nozzle flow, which leads to a lower value of C_d^{Core}. The impact of installation on C_d^{Core} is very large across the descent phase, with differences in C_d^{Core} between the installed and isolated configurations increasing with flight Mach number. The installation effects need to be accounted for from a performance modelling perspective and require good estimates of C_d^{Core} at idle conditions. The predictions of C_d^{Core} are vital for the performance evaluation of the compressor and turbine operating conditions [7].

At the top of descent (M_1), the C_d^{Core} for the isolated engine without a pylon is $\simeq 25\%$ lower compared to the isolated engine with a pylon. The differences in C_d^{Core} between the isolated engine with and without a pylon are $\simeq 23 - 26\%$ between the top of descent (M_1) and a flight condition close to the end of descent (M_5). This difference decreases to $\simeq 8.8\%$ at the end of descent (M_6). The pylon "shields" the core nozzle from the suppression effects of the freestream, which results in higher values of C_d^{Core} for the isolated engine configuration with the pylon as compared to the isolated engine without a pylon. The bypass jet does not fully shield the core nozzle from suppression effects of the freestream at high Mach numbers [37], and the static pressure exerted by the post-exit streamtube propagates to the core afterbody which results in the suppression of the core nozzle discharge coefficient.

The effect of the pylon mitigates the effect of freestream suppression in the region directly underneath it. Thus, the inclusion of the pylon brings about an asymmetry in the static pressure distribution downstream of the core nozzle, which reduces the core nozzle base pressure [64], and leads to higher mass flows from the core nozzle.

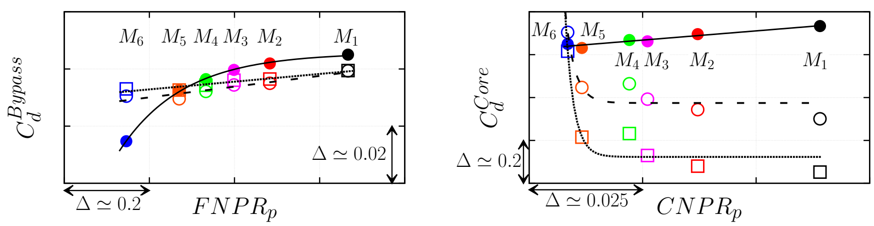

(a) (b)

Figure 7: Variation of the discharge coefficient with the corresponding prescribed nozzle pressure ratio along the descent profile. (a) Bypass nozzle and (b) core nozzle: for the aero-engine installed on the airframe (●), isolated engine with the pylon (○), and the isolated engine without pylon (□). The solid, dashed and dotted lines are the curves of best fit through the data points.

At the top of descent (M_1), the isolated engine without a pylon has a higher static pressure on the core after-body and plug as compared to the other cases (Fig. 8(a)). With the inclusion of the pylon, the static pressure distribution is slightly altered on the core cowl after-body and the core plug, and small changes are observed in the vicinity of the top-line of the nacelle after-body and pylon intersection region (dashed box in Fig. 8(b)). The static pressure on the core cowl after-body and plug for the installed aero-engine is lower compared to the corresponding isolated engines. The static pressure is reduced on the inboard side (Fig. 8(c)) as compared to the outboard side (Fig. 8(d)), as a result of the inboard suction peak caused by the flow acceleration between the engine and the fuselage. Furthermore, the flow acceleration on the underside of the aircraft wing leads to lower values of C_p^{mod} on the core after-body on both the inboard and outboard sides of the installed engine. Lower values of C_p^{mod} are also observed on the pylon surface downstream of the core nozzle exit, and this leads to an increase in C_d^{Core} values compared to the isolated cases. The effect of installation, together with the gully flow effect between the engine and the wing results in a higher value of bypass nozzle discharge coefficient ($\Delta C_d^{Bypass} \simeq 0.56\%$) and core nozzle discharge coefficient ($\Delta C_d^{Core} \simeq 43\%$) for the installed aero-engine as compared to the isolated case with the pylon.

For the isolated engine without the pylon at the end of descent, M_6 (Fig. 9(a)), the freestream suppression leads to higher static pressure at the core nozzle exit,

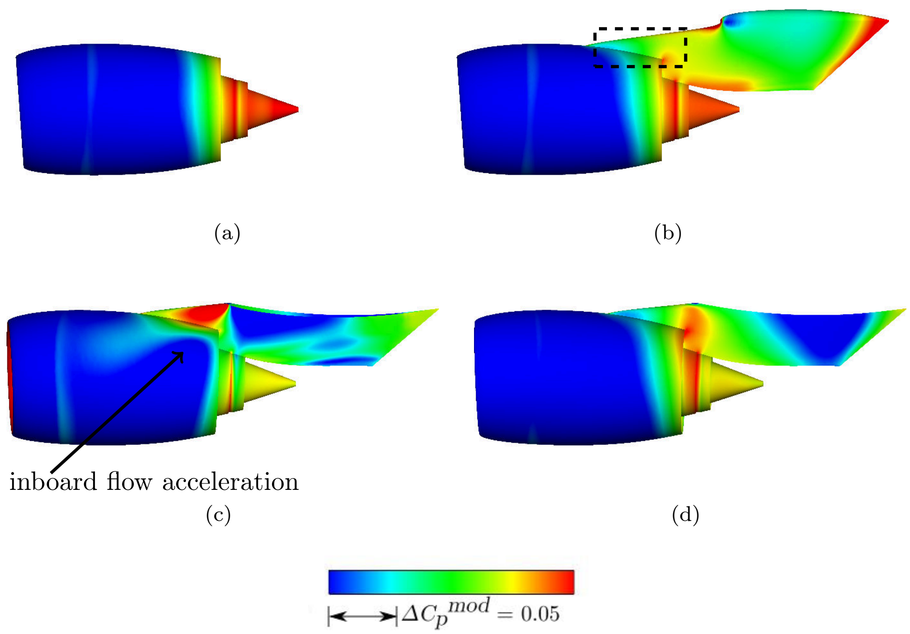

Figure 8: Contours of C_p^{mod} at the top of descent (M_1) for (a) isolated engine without the pylon, (b) isolated engine with the pylon, (c) inboard side of the installed engine, and (d) outboard side of the installed engine. Flow is from left to right in these images.

which results in a lower efflux from the core (Fig. 10(d)). This results in lower values of C_d^{Core} by $\simeq 8.8\%$ compared to the isolated engine with the pylon, and lower values of C_p^{mod} on the core after-body (Fig. 9(b)). At the end of descent (M_6), the aircraft is operating at a lower Mach number and an increased incidence angle. The increased static pressure distribution from the wing can be observed on the top-line of the nacelle after-body (the dashed box in Fig. 9(c)) and the exhaust after-body (Fig. 9(c) and Fig. 9(d)). This leads to flow suppression of the bypass and core nozzles, and consequently, a lower discharge coefficient for the installed cases as compared to the isolated engine with the pylon ($\Delta C_d^{Bypass} \simeq -1.6\%, \Delta C_d^{Core} \simeq -5.4\%$). The reduced effect of the engine-airframe interaction can be observed by examining the contours of C_p^{mod} on the inboard side of the nacelle at M_6 (Fig. 9(c)) as compared to its counterpart at the highest Mach number, M_1 (Fig. 8(c)).

To further elucidate the impact of installation and the aerodynamic effects on the core nozzle discharge for the three levels of integration considered, the normalised streamwise mass flux $f = \rho U_x/\dot{m}^{Core}$ at operating conditions M_1 and M_6 is considered (Fig. 10). The range of contour levels is centred around the mean value of the

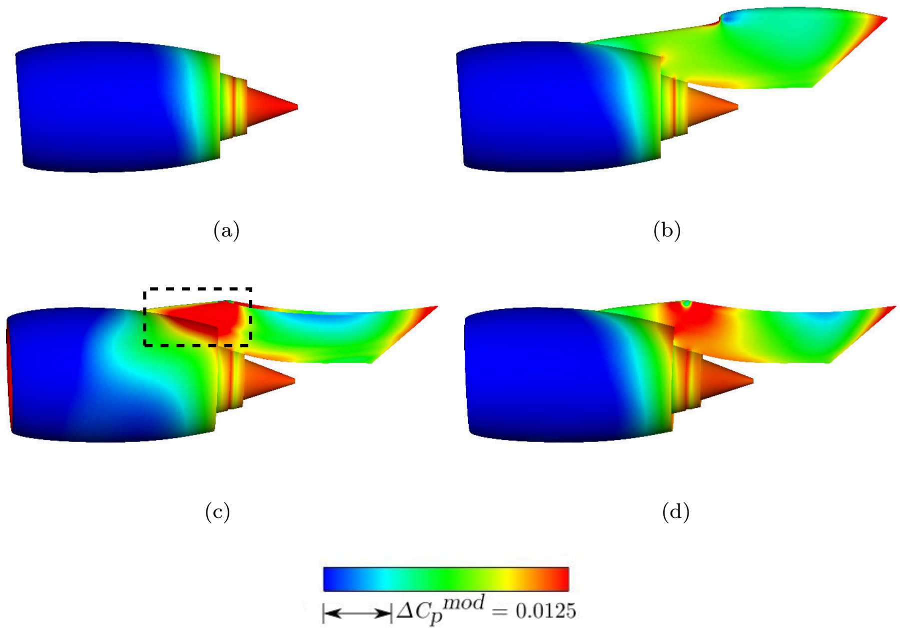

Figure 9: Contours of C_p^{mod} at the end of descent (M_6) for (a) isolated engine without the pylon, (b) isolated engine with the pylon, (c) inboard side of the installed engine, and (d) outboard side of the installed engine. Flow is from left to right in these images.

normalised flux ($0 \leqslant \dfrac{f - f_{min}}{f_{max} - f_{min}} \leqslant 1$) to accommodate the large disparity in the core mass flow between the various integration levels, and to highlight the asymmetry of the distributions. An asymmetric distribution across the horizontal midplane is observed for the isolated case without the pylon on account of the incidence angle at M_1 (Fig. 10(a)) and M_6 (Fig. 10(d)). At the top of descent (M_1), for the isolated aero-engine with a pylon, the mass flux directly below the pylon is lower compared to that around the sides as a result of higher static pressure downstream of the core exit plane (Fig. 10(b)). Flow separation is observed on the pylon heat-shield and the core plug for this operating condition, which leads to flow blockage near the core nozzle top-line. However, for this configuration at the end of descent (M_6), the pylon mitigates the freestream suppression, which leads to higher values of mass flux directly beneath it (Fig. 10(e)). For the installed configurations, the impact of the engine-airframe interaction is discernible at both M_1 and M_6, with the mass flux distribution on the inboard side higher compared to the outboard side. On account of the "gully effect" [30], higher mass flux distribution is observed close to the pylon junction on the inboard side (Fig. 10(c) and Fig. 10(f)).

Thus, a multitude of aerodynamic effects influences the bypass and core nozzle

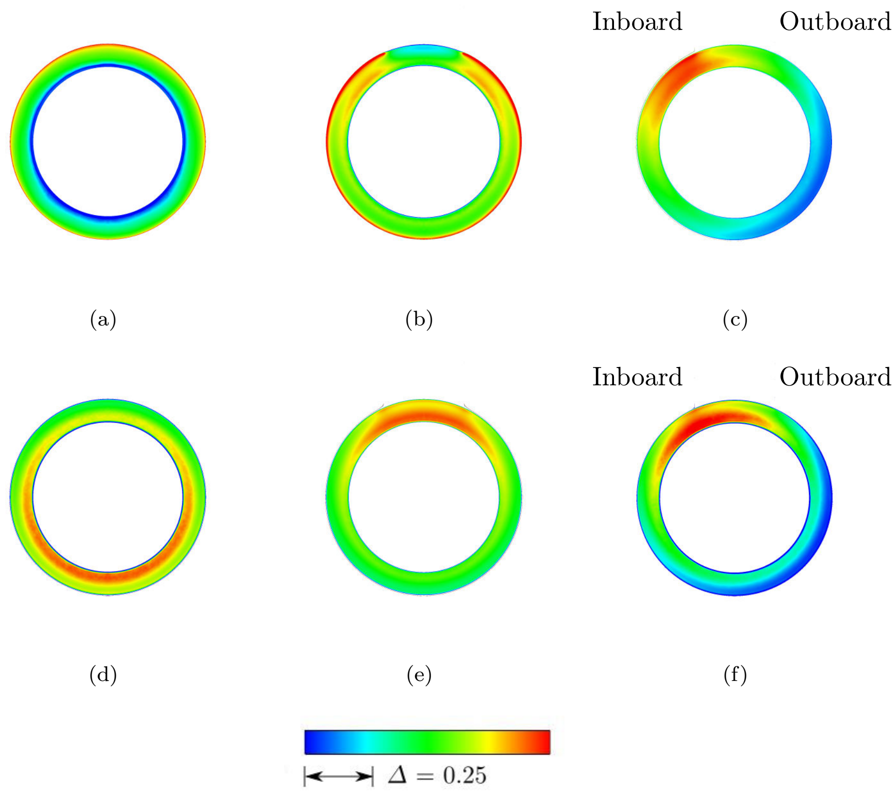

Figure 10: Contours of normalised streamwise mass flux at the core nozzle exit plane at the top of descent (M_1) - (a) - (c), and at the end of descent (M_6) - (d) - (f). Isolated engine without the pylon - (a), (d), Isolated engine with the pylon - (b), (e), and installed engine (c), (f). Images captured from a point downstream of the engine, looking upstream.

discharge coefficient, which leads to a large variation not only along the descent profile, but also across the various levels of integration. The impact of installation augments the C_d^{Core} values across a large part of the descent profile compared to the isolated engines, while the impact of installation on C_d^{Bypass} is relatively small.

3.3. Sensitivity of the discharge coefficient to the incidence angle

Across the idle descent range, the incidence angle of the aircraft changes, and to ascertain the effect of the incidence angle on the exhaust metrics, simulations were performed across a range of $\Delta\alpha \simeq 2.5°$ at the four operating points - M_1, M_2, M_4 and M_6. The NPR_p of the bypass and core nozzles were held constant at a given operating point as the incidence angle was varied. The variation of the bypass and core nozzle discharge coefficient with incidence is reported only for the installed engine as the impact of incidence for the isolated engines was minimal. For the isolated engines, $\dfrac{d(C_d^{Bypass})}{d(\alpha)}$ and $\dfrac{d(C_d^{Core})}{d(\alpha)}$ was $\lesssim 0.0005$ and $\lesssim 0.0055$, respectively.

For the installed engine, C_d^{Bypass} and C_d^{Core} decrease monotonically with increasing incidence (Fig. 11). An increase in the incidence angle leads to a higher wing loading. The rise in the static pressure from the pressure side of the wing acts on the exhaust after-body, which suppresses the flow from the nozzles [13], and leads to lower values of the discharge coefficient at higher incidence angles. As the Mach number increases, the adverse effects of freestream suppression are counteracted by the increase in the prescribed fan nozzle pressure ratio and engine-airframe interaction, which results in higher values of C_d^{Bypass} (Fig. 11(a)). Across the descent phase, $\dfrac{d(C_d^{Bypass})}{d(\alpha)}$ varied between 0.003 and 0.006.

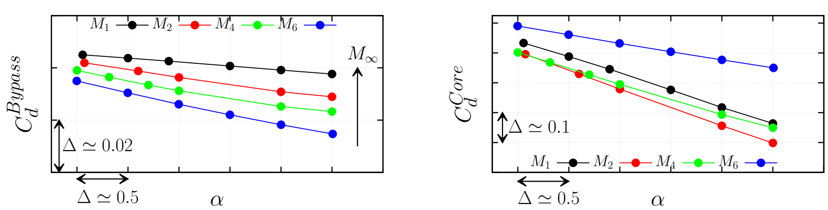

(a) (b)

Figure 11: Variation of the discharge coefficient with incidence angle for (a) the bypass nozzle, and (b) the core nozzle for the four operating points along the descent profile for the installed configuration.

The variation of C_d^{Core} with incidence angle is monotonic at a given value of M_∞, with a linear decrease in C_d^{Core} with incidence angle on account of the increased wing loading on the core after-body (Fig. 11(b)). For flight conditions M_1, M_2 and M_4, $\dfrac{d(C_d^{Core})}{d(\alpha)}$ is $\simeq 0.12$, and for M_6, $\dfrac{d(C_d^{Core})}{d(\alpha)}$ is $\simeq 0.056$. The core nozzle discharge coefficient is influenced not only by the pressure field from the wing at incidence and the freestream suppression effects [65], but also by the bypass jet flow suppression effect on core after-body trailing edge base pressure [36]. Thus, several competing mechanisms affect the static pressure to which the core nozzle discharges, which results in a non-monotonic behaviour of C_d^{Core} with flight Mach number [13].

For the highest and the lowest flight Mach numbers considered, an increase in the incidence angle leads to an increase in the static pressure on the exhaust systems on both the inboard and the outboard sides, as seen by the dashed box in Fig. 12(b) and Fig. 12(d) at flight condition M_1. The increased incidence angle counteracts the impact of the engine-airframe interaction on the inboard side of the aero-engine as witnessed by the increase in C_p^{mod} values on the nacelle after-body

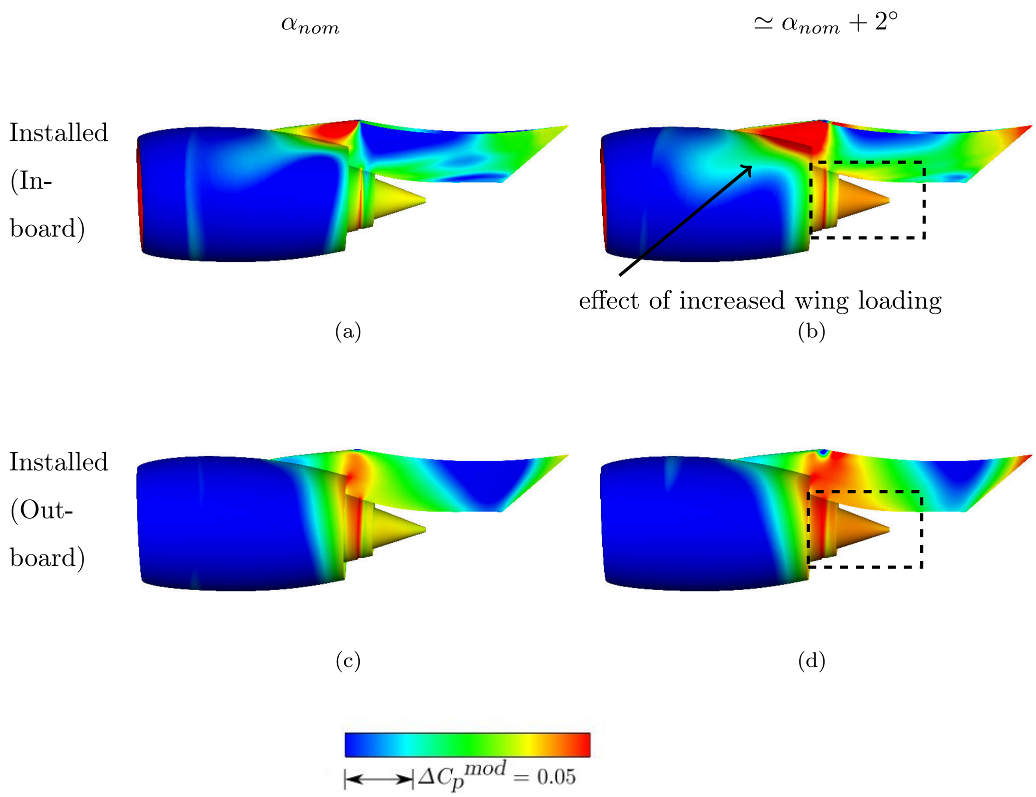

Figure 12: Contours of C_p^{mod} at the top of descent (M_1) for the installed aero-engine, showing changes in the pressure distribution with incidence. Subfigures (a), (c) correspond to α_{nom}, and (b), (d) correspond to $\simeq \alpha_{nom} + 2°$.

and the pylon. The contour levels of C_p^{mod} in Fig. 12 and Fig. 13 were chosen to highlight the impact of incidence at the respective flight conditions. Due to the larger axial overlap of the swept wing, the static pressure field has a larger impact on the inboard side (Fig. 12(b), Fig. 13(b)) as compared to the outboard side (Fig. 12(d), Fig. 13(d)). These effects are more benign at the end of descent (M_6) (Fig. 13(b)), where the engine-airframe interaction is reduced compared to the higher Mach number cases. On the outboard side, an increase in C_p^{mod} is observed on the pylon underneath the wing leading edge and on the exhaust after-body with an increase in the incidence angle (Fig. 12(d), Fig. 13(d)). The increased static pressure suppresses the flow from the nozzles, which leads to lower discharge coefficients with increasing incidence [13].

Thus, the discharge coefficients for the bypass and core nozzles decrease monotonically with an increase in the incidence angle for the installed engines. The higher static pressure generated by the wing on the core cowl after-body leads to

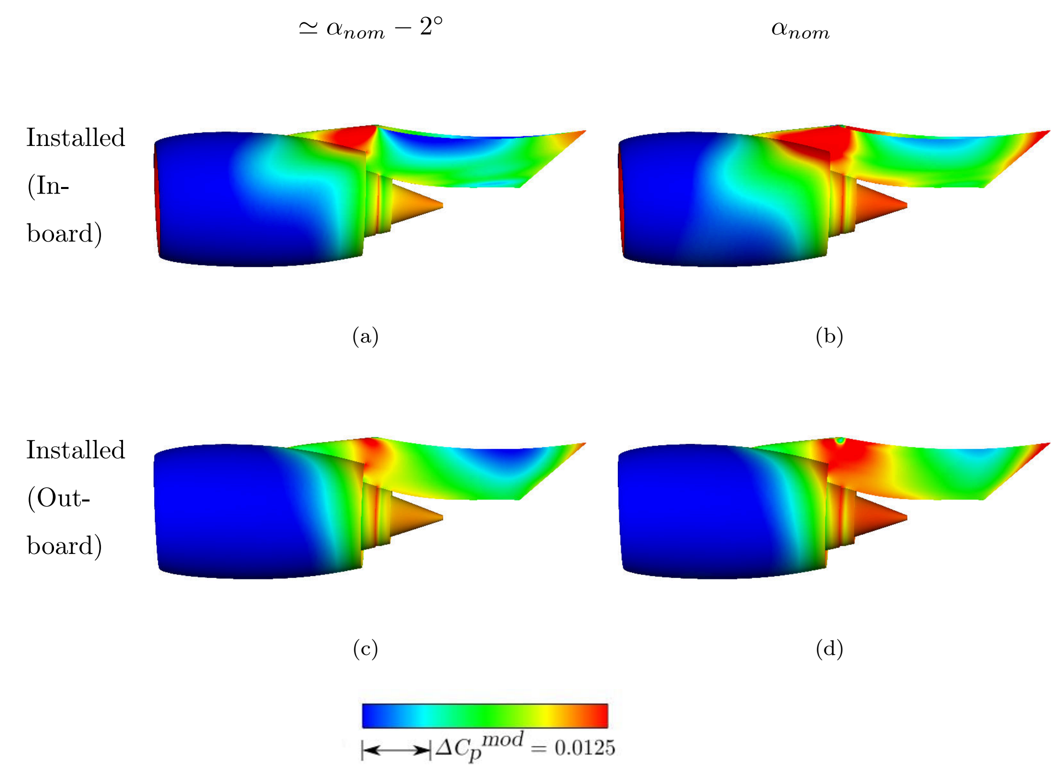

Figure 13: Contours of C_p^{mod} at the end of descent (M_6) for the installed aero-engine, showing changes in the pressure distribution with incidence. Subfigures (a), (c) correspond to $\simeq \alpha_{nom} - 2°$, and (b), (d) correspond to α_{nom}.

the suppression of the nozzle efflux, which results in lower values of the discharge coefficient. For a given incidence angle, C_d^{Bypass} increases monotonically with M_∞, while the variation of C_d^{Core} is non-monotonic as it is influenced by the bypass flow.

3.4. Sensitivity of the discharge coefficient to nozzle pressure ratio

The sensitivity of the discharge coefficients to small changes in the bypass and core nozzle pressure ratio about the nominal points was investigated at idle descent conditions for the installed and the isolated engine with the pylon. For these simulations, by independently varying the $FNPR_p$ and $CNPR_p$, while keeping the $CNPR_p$ and $FNPR_p$ constant, respectively, the impact of the extraction ratio on the metrics is investigated, albeit implicitly. The incidence angle is held constant at α_{nom} as the nozzle pressure ratios were varied.

3.4.1. Sensitivity of the discharge coefficient to fan nozzle pressure ratio

The sensitivity of the discharge coefficients to small changes in $FNPR_p$ is considered for four operating conditions across the descent profile. In Fig. 14, the values of bypass and core nozzle discharge coefficient are normalised by the corresponding nominal values evaluated along the descent profile to highlight the sensitivity of the metrics to changes in $FNPR_p$. The $FNPR_p$ at which the normalised values of discharge coefficient for the installed and isolated configurations coincide corresponds to the nominal value of $FNPR_p$ at the specified flight condition as shown in Fig. 1. In general, C_d^{Bypass} increases monotonically with an increase in $FNPR_p$ across the descent phase for both the installed and isolated configurations (Fig. 14(a)). The bypass nozzle remains unchoked for the range of $FNPR_p$ considered here. The maximum difference in C_d^{Bypass} between the installed and isolated configurations is $\lesssim 2.5\%$ at low $FNPR_p$, and the difference decreases to $\lesssim 0.4\%$ as $FNPR_p$ is increased. The impact of installation on C_d^{Bypass} with increasing $FNPR_p$ is generally low.

An increase in $FNPR_p$ leads to a monotonic decrease in C_d^{Core} across the descent phase for both the installed and the isolated configurations (Fig. 14(b)). The effect of installation reduces the sensitivity of $\frac{d(C_d^{Core}/C_{d,nom}^{Core})}{d(FNPR_p)}$. For example, at the top of descent (M_1), $\frac{d(C_d^{Core}/C_{d,nom}^{Core})}{d(FNPR_p)} \simeq -0.31$ for the isolated engine with the pylon, and for the installed configuration, $\frac{d(C_d^{Core}/C_{d,nom}^{Core})}{d(FNPR_p)} \simeq -0.18$. The relative impact of installation is reduced across the descent profile. At mid-point of the descent (M_4), $\frac{d(C_d^{Core}/C_{d,nom}^{Core})}{d(FNPR_p)}$ for the isolated and the installed cases are $\simeq -0.52$ and $\simeq -0.35$, respectively. At the end of descent (M_6), the impact of installation is reduced, with $\frac{d(C_d^{Core}/C_{d,nom}^{Core})}{d(FNPR_p)}$ being similar for the isolated and installed configurations.

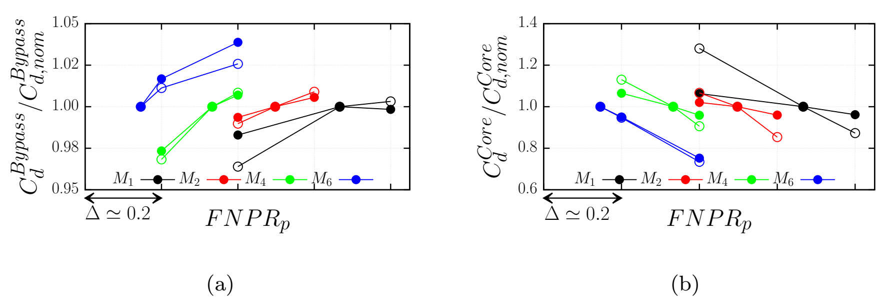

Figure 14: Variation of (a) the $C_d^{Bypass}/C_{d,nom}^{Bypass}$ with $FNPR_p$, and (b) the $C_d^{Core}/C_{d,nom}^{Core}$ with $FNPR_p$ for four different operating points for the aero-engine in the installed configuration (●) and isolated engine with the pylon (○) at constant $CNPR_p$.

The bypass jet streamtube curves radially inwards in a concave manner towards the core after-body and is aligned with the thrust axes downstream of the core plug. The concavity of the streamtube due to flow turning induces a static pressure rise on the core cowl after-body and the core plug. Thus, at a given $FNPR_p$, the concavity of the post-exit bypass jet affects the static pressure to which the core nozzle discharges, and thus, C_d^{Core} is influenced by $FNPR_p$. At a higher $FNPR_p$, the bypass nozzle efflux increases, and together with the higher turning rate of the post-exit streamtube, leads to a further increase in the static pressure over the core cowl after-body and core plug [37]. The core mass flow is suppressed further, and this results in lower C_d^{Core} values at higher $FNPR_p$.

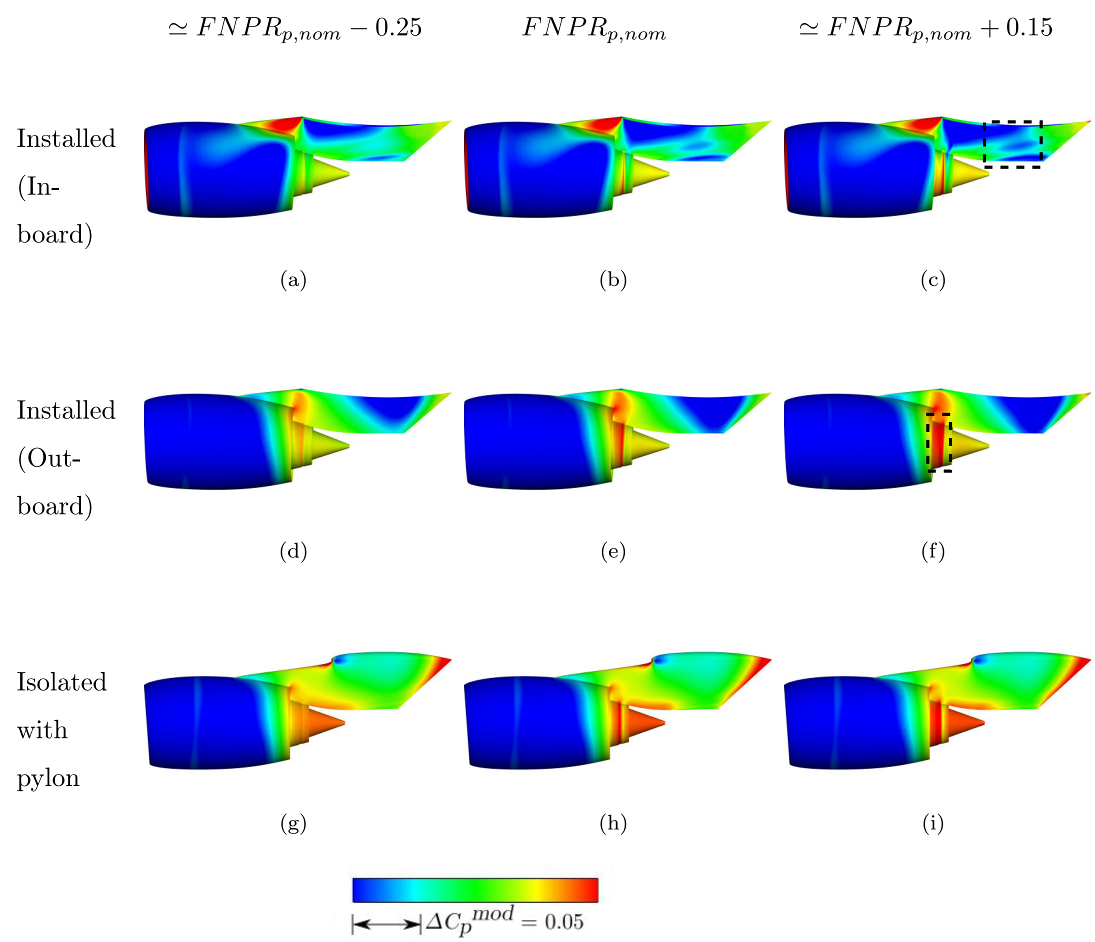

Figure 15: Contours of C_p^{mod} at the top of descent (M_1) for the installed engine and isolated engine with the pylon, showing changes in pressure distribution with increasing $FNPR_p$. Subfigures (a), (d) and (g) correspond to $\simeq FNPR_{p,nom} - 0.25$; (b), (e) and (h) correspond to $FNPR_{p,nom}$, and (c), (f) and (i) correspond to $\simeq FNPR_{p,nom} + 0.15$.

At the start of descent (M_1), an increase in $FNPR_p$ leads to higher values of C_p^{mod} on the core cowl after-body and the core plug as a result of the increased efflux from the bypass jet (Fig. 15). Higher values of C_p^{mod} are observed on the exhaust system for the isolated cases (Fig. 15(g) - Fig. 15(i)) as compared to the installed configuration (Fig. 15(a) - Fig. 15(f)) on account of the freestream suppression effects. The static pressure on the core cowl after-body progressively increases as $FNPR_p$ is increased for both the configurations. For the installed engine, lower values of C_p^{mod} are observed on the inboard side (Fig. 15(a) - Fig. 15(c)) as compared to the outboard side (Fig. 15(d) - Fig. 15(f)) due to the engine-airframe interaction. Changes in the C_p^{mod} distribution are also observed on the inboard side of the pylon (dashed box in Fig. 15(c)). Higher values of C_p^{mod} are observed on the core cowl after-body on the outboard side (dashed box in Fig. 15(f)) on increasing $FNPR_p$. Similar behaviour is observed at other flight conditions, with the increased $FNPR_p$ resulting in higher values of C_p^{mod} on the core cowl after-body.

3.4.2. Sensitivity of the discharge coefficient to core nozzle pressure ratio

The sensitivity of the discharge coefficients to small changes in $CNPR_p$ is investigated at the top of descent (M_1) and the end of descent (M_6). In Fig. 16, the values of bypass and core nozzle discharge coefficient are normalised by the corresponding nominal values evaluated along the descent profile to highlight the sensitivity of the metrics to changes in $CNPR_p$. The $CNPR_p$ at which the normalised values of discharge coefficient for the installed and isolated configurations coincide corresponds to the nominal value of $CNPR_p$ at the specified flight condition as shown in Fig. 1. C_d^{Bypass} is nearly invariant with an increase in $CNPR_p$ at either end of the descent profile. The ratio of C_d^{Bypass} to the nominal value $C_{d,nom}^{Bypass}$ decreases marginally with an increase in $CNPR_p$ (Fig. 16(a)). C_d^{Bypass} is nearly invariant with changes in $CNPR_p$.

In general, $C_d^{Core}/C_{d,nom}^{Core}$ increases monotonically with an increase in $CNPR_p$ at both M_1 and M_6 (Fig. 16(b)). For the range of $CNPR_p$ considered in Fig. 16(b), $CNPR_p < \lambda_{crit}$. The increased core nozzle pressure ratio increases the core nozzle efflux and mitigates the suppression effects from the freestream and the bypass jet, which leads to an in C_d^{Core} for both the installed and isolated configurations. At M_1, the effect of installation is to reduce the sensitivity of $C_d^{Core}/C_{d,nom}^{Core}$ by a factor of two. For the isolated engine at M_1, an increase in $\Delta CNPR_p \simeq 0.1$, results in an increase of C_d^{Core} by $\simeq 2.4$ times the nominal value, while for the installed case, the increase is $\simeq 1.2$ times the nominal value. At the end of descent (M_6), $C_d^{Core}/C_{d,nom}^{Core}$ is similar for the installed and isolated configurations, with the impact of installation being reduced at the end of descent. Thus, an increase in the extraction ratio increases the C_d^{Bypass} and decreases the C_d^{Core} for the range of nozzle pressure ratios considered here.

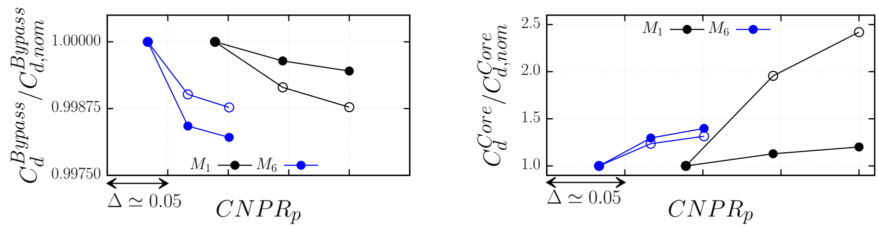

(a) (b)

Figure 16: Variation of (a) the $C_d^{Bypass}/C_{d,nom}^{Bypass}$ with $CNPR_p$, and (b) the $C_d^{Core}/C_{d,nom}^{Core}$ with $CNPR_p$ for the installed configuration (●) and isolated engine with the pylon (○) at constant $FNPR_p$.

At the top of descent (M_1), an increase in $CNPR_p$ of $\simeq 0.1$ compared to the nominal value, leads to higher values of C_p^{mod} on the core plug as a result of the increased mass efflux from the core nozzle on both the inboard (dashed box in Fig. 17(b)) and outboard sides (Fig. 17(d)). Minor changes in C_p^{mod} are also observed on the inboard side of the pylon for the installed aero-engine. The engine-airframe interaction on the inboard side leads to lower C_p^{mod} values for the installed case as compared to the outboard side. For the isolated cases (Fig. 17(e) - Fig. 17(f)), suppression effects from the freestream Mach number result in higher values of C_p^{mod} on the core after-body as compared to the installed cases. When $CNPR_p$ is increased, higher values of C_p^{mod} are observed on the core plug (Fig. 17(f)) due to the higher efflux from the core nozzle. Similar behaviour is observed at the end of descent (M_6), with an increase in C_p^{mod} on the core plug for both the installed and the isolated configurations.

3.5. Reduced-order model to predict the core discharge coefficient at idle descent conditions

The performance evaluation of an aero-engine is usually performed at ground static conditions for the engine in the isolated configuration [66, 67]. However, as seen in previous sections, installation effects play a vital role for an aero-engine in flight, and the aerodynamic interactions with the airframe need to be accounted for when determining the performance characteristics. The impact of installation on C_d^{Bypass} is relatively small across the idle descent profile, with a maximum difference of $\simeq 1.6\%$ observed between the installed and isolated engines. However,

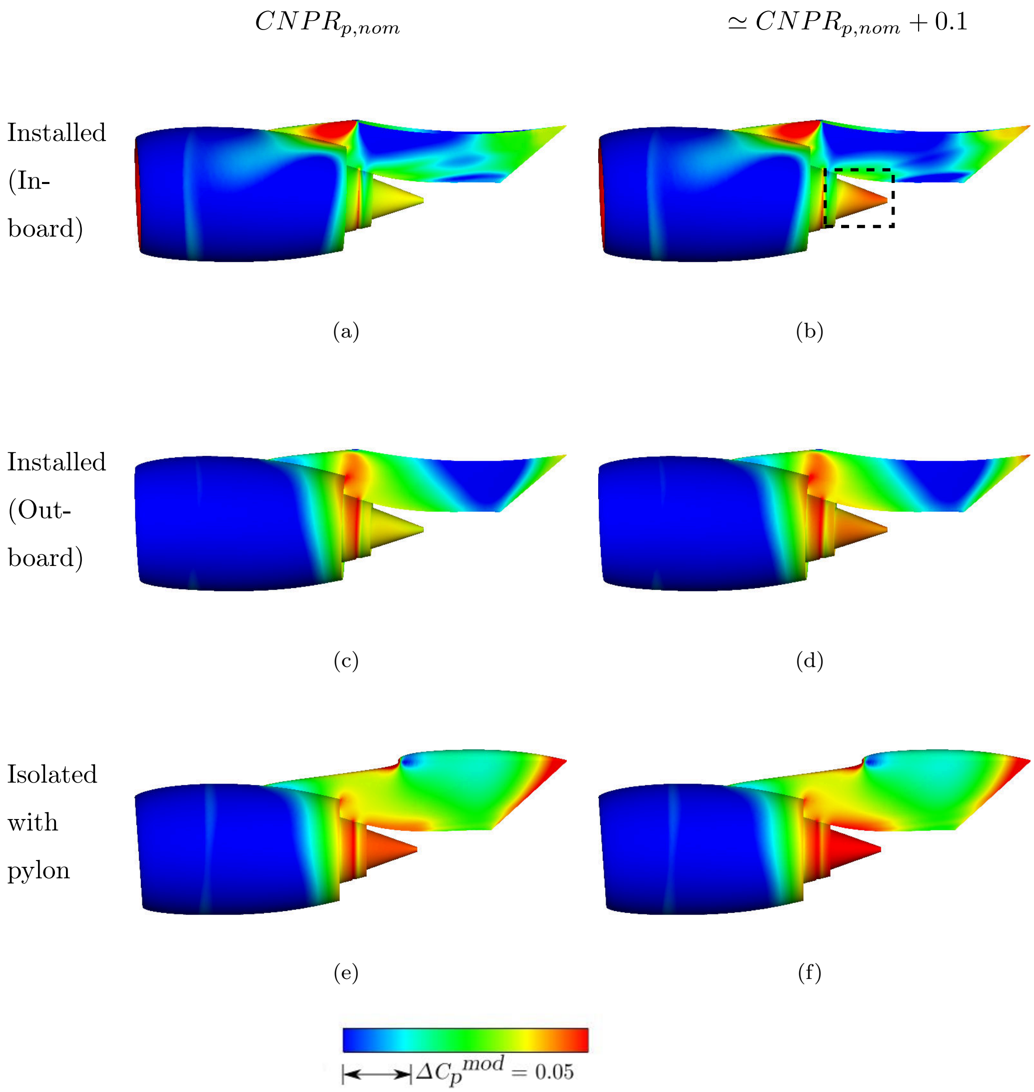

Figure 17: Contours of C_p^{mod} at the top of descent (M_1) for the installed engine and isolated engine with the pylon, showing changes in pressure distribution with increasing $CNPR_p$. Subfigures (a), (c) and (e) correspond to $CNPR_{p,nom}$, and (b), (d) and (f) correspond to $\simeq CNPR_{p,nom} + 0.1$.

the differences in the core nozzle discharge coefficient between the installed and isolated configurations are significant. At the top of descent (M_1), the difference between the installed and the isolated configuration with the pylon was $\Delta C_d^{Core} \simeq$ 43%, while at the end of descent (M_6), the difference was $\Delta C_d^{Core} \simeq -5.4\%$. C_d^{Core} can affect engine re-matching, and cause a change in the engine operating point and other parameters such as compressor stall margins and shaft speeds. Furthermore, the uncertainties associated with the predictions of core mass flow are large at idle conditions as they are typically extrapolated from above-idle conditions [7, 8]. Thus, it is essential to obtain good estimates of the installed C_d^{Core}, which can be used to derive the performance characteristics of future aero-engines in a systems-level modelling tool [68].

A combination of factors influences the static pressure field on the exhaust system of an installed engine, such as the design of the nacelle, exhaust system and pylon, installation position of the engine, pitch and toe angles, flight Mach number (M_∞), incidence angle (α), and the prescribed nozzle pressure ratios (NPR_p). On account of these effects, the bypass and core nozzles discharge to a pressure field which is different from the ambient pressure. Otter *et al.* [37] showed that under cruise conditions, the exhaust discharge coefficients can be modelled based on the "effective" pressure ratio to account for the suppression effects of the freestream and the bypass jet. The aim here is to develop a correlation between the core nozzle discharge coefficient and the effective pressure ratio to account for the effect of installation and the operating conditions. This will enable the development of a ROM based on a limited number of simulations, which can then be used in engine performance simulations.

An estimation of the C_d^{Core} for the installed HBR aero-engine is developed by correlating it to an "effective" pressure around the base of the core nozzle exit [37, 48]. A circumferentially-averaged value of the core nozzle exit base static pressure (p_b^{Core}) is considered to obtain the effective core nozzle pressure ratio ($CNPR_e = \frac{P_o^{Core}}{p_b^{Core}}$). The subscript $()_e$ denotes it is an effective pressure ratio to differentiate it from the prescribed nozzle pressure ratio $()_p$ at the nozzle inlets based on the freestream static pressure. Based on the simulations for the various levels of engine integration at idle descent conditions, sensitivity to incidence angle and nozzle pressure ratios, the effective core discharge coefficient ($C_{d,e}^{Core}$) can be related to the $CNPR_e$ (Fig. 18). The correlation takes the form of an exponential function (Eq. 9). One of the objectives of examining this correlation is to assess the overall combined effects of flight Mach number, incidence, installation and changes to the nozzle pressure ratios on the relationship between $C_{d,e}^{Core}$ with $CNPR_e$. As expected, it substantially reduces the variation to a standard $C_d^{Core} - CNPR_p$ relationship. However, at low $CNPR_e$ there is still some sensitivity to the flight Mach number. Thus, the large variations in C_d^{Core} across the three engine configurations and operating conditions can be modelled as a linear function relating the core mass flow with the effective nozzle pressure ratio, and this enables the derivation of a ROM.

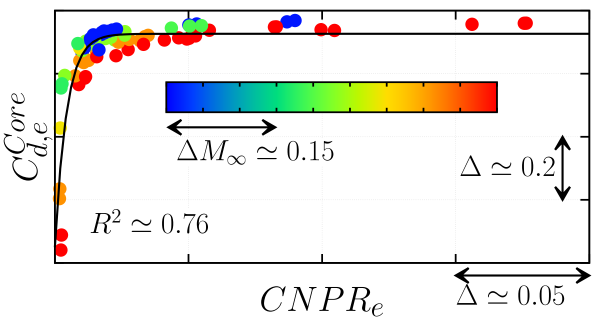

Figure 18: Variation of $C_{d,e}^{Core}$ with $CNPR_e$ across the idle descent conditions for the three configurations considered. The black line is an exponential function fit (Eq. 9) through the data points, which are coloured by flight Mach number.

Here, the effective core discharge coefficient $C_{d,e}^{Core}$ is defined as,

$$C_{d,e}^{Core} = \frac{\dot{m}^{Core}}{\left(\dfrac{\dot{m}}{A}\right)_e^{ideal} A_{throat}^{Core}} \tag{3}$$

where, $\left(\dfrac{\dot{m}}{A}\right)_e^{ideal}$ is computed based on $CNPR_e$ (or $\lambda_e = \dfrac{P_o^{Core}}{p_b^{Core}}$), and A_{throat}^{Core} is the core nozzle throat area:

$$\left(\frac{\dot{m}}{A}\right)_e^{ideal} = P_o^{Core}\left(\frac{1}{\lambda_e}\right)^{\dfrac{1}{\gamma}}\sqrt{\frac{2\gamma}{(\gamma-1)RT_o^{Core}}\left(1-\left(\frac{1}{\lambda_e}\right)^{\dfrac{\gamma-1}{\gamma}}\right)} \tag{4}$$

Eq. 4 is similar to Eq. 2, with the "effective" quantities used for the computations instead of the prescribed quantities. The following procedure is used to determine the core discharge coefficient from the flight conditions - $M_\infty, p_\infty, \alpha$ and the aero-thermodynamic variables for the core nozzle - P_o^{Core}, and T_o^{Core}. Here, M_∞, p_∞ and α would be known from the aircraft's descent profile, while P_o^{Core} and T_o^{Core} would be known from the engine cycle data.

The normalised mean static pressure at the core nozzle exit base $\left(\dfrac{p_b^{Core}}{p_\infty}\right)$ for the installed aero-engine is obtained as a function of the flight Mach number and incidence angle in a two-step process. First, the variation of the normalised core nozzle base pressure $\left(\dfrac{p_{b,NPR}^{Core}}{p_\infty}\right)$ is obtained for the nominal points along the descent profile and the small variations in the nozzle pressure ratio as a function of the flight Mach number (Fig. 19):

$$\frac{p_{b,NPR}^{Core}}{p_\infty} = f(M_\infty) = a_0\ M_\infty^{b_0} + c_0 \tag{5}$$

where, a_0, b_0 and c_0 are constants. Thus, for a given M_∞, $\left(\frac{p_{b,NPR}^{Core}}{p_\infty}\right)$ can be determined. It may be noted that $f()$ is used in a notional sense.

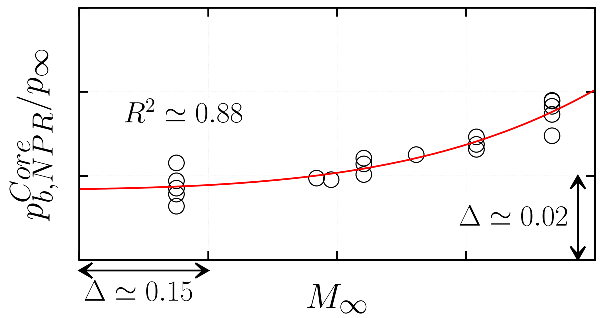

Figure 19: Variation of $\left(\frac{p_{b,NPR}^{Core}}{p_\infty}\right)$ with M_∞. The regression line (in red) is obtained for the data presented in section 3.

Secondly, given the large variation in C_d^{Core} values with incidence (Fig. 11(b)), the changes brought about by the aircraft's wing loading are accounted for separately. The differences between the normalised mean static pressure at the base of the core nozzle at the various incidence angles and the incidence angle at the nominal operating point are obtained as a function of M_∞ and α, with the equation taking the form of a polynomial function (Eq. 6).

$$\begin{aligned}\frac{\Delta p_{b,\alpha}^{Core}}{p_\infty} &= f(M_\infty, \alpha) \\ &= a_1 + b_1\alpha + c_1 M_\infty + d_1\alpha^2 + e_1\alpha M_\infty \\ &+ f_1 M_\infty^2 + g_1\alpha^2 M_\infty + h_1\alpha M_\infty^2 + i_1 M_\infty^3\end{aligned} \tag{6}$$

where, a_1, $b_1 ... i_1$ are constants.

The cumulative normalised mean static pressure at the base of the core nozzle $\left(\frac{p_b^{Core}}{p_\infty}\right)$ for the installed engine is obtained by:

$$\frac{p_b^{Core}}{p_\infty} = \frac{p_{b,NPR}^{Core}}{p_\infty} + \frac{\Delta p_{b,\alpha}^{Core}}{p_\infty} \tag{7}$$

Thus, for a given flight condition and the corresponding ambient static pressure (p_∞), the cumulative mean static pressure at the base of the core nozzle (p_b^{Core}) can be obtained. $CNPR_e$ or λ_e is then determined from P_o^{Core} and p_b^{Core} by:

$$\lambda_e = \frac{P_o^{Core}}{p_b^{Core}} \tag{8}$$

The corresponding value of the effective core nozzle discharge coefficient ($C_{d,e}^{Core}$) is determined from the exponential function in Eq. 9 relating $C_{d,e}^{Core}$ and $CNPR_e$ (Fig. 18).

$$C_{d,e}^{Core} = f(CNPR_e) = a_2 - b_2 e^{-c_2 \; CNPR_e} \tag{9}$$

where, a_2, b_2 and c_2 are constants.

From the value of $C_{d,e}^{Core}$, the mass flow through the core nozzle per unit core nozzle throat area $\left(\frac{\dot{m}^{Core}}{A_{throat}^{Core}}\right)$ is determined from $CNPR_e$ (or λ_e), $T_o^{Core}, P_o^{Core}, \gamma$, and R.

$$\frac{\dot{m}^{Core}}{A_{throat}^{Core}} = C_{d,e}^{Core} \left(\frac{\dot{m}}{A}\right)_e^{ideal} \tag{10}$$

where, $\left(\frac{\dot{m}}{A}\right)_e^{ideal}$ corresponds to the isentropic equation based on the effective core nozzle pressure ratio, and is computed from Eq. 4. Note that the mass flow from the exit nozzle is expressed as $\left(\frac{\dot{m}^{Core}}{A_{throat}^{Core}}\right)$, and the method can be used without directly requiring a specification for the core nozzle throat area.

Based on the obtained core mass flow per unit area, the core discharge coefficient is estimated for the prescribed nozzle pressure ratio ($CNPR_p$ or λ_p) from $\left(\frac{\dot{m}^{Core}}{A_{throat}^{Core}}\right)$, $\lambda_p, T_o^{Core}, P_o^{Core}, \gamma$ and R. The related equation is:

$$C_{d,ROM}^{Core} = \frac{\dfrac{\dot{m}^{Core}}{A_{throat}^{Core}}}{\left(\dfrac{\dot{m}}{A}\right)_p^{ideal}} \tag{11}$$

where, $\left(\frac{\dot{m}}{A}\right)_p^{ideal}$ is computed from Eq. 2, and $C_{d,ROM}^{Core}$ is the core discharge coefficient obtained from the reduced-order model (ROM). To evaluate if the reduced-order model provided reasonable estimates, the computed C_d^{Core} values were compared with the estimated values ($C_{d,ROM}^{Core}$) across the idle descent range (Fig. 20) for the installed configuration investigated in section 3. The estimated values are in reasonable agreement with the computed values, with $r \simeq 0.968$, where r is the Pearson's correlation coefficient. The standard deviation ($\sigma_{\Delta C_d^{Core}} = \sqrt{\frac{1}{N}\sum_{i=1}^{N}(\Delta C_d^{Core})^2}$) of the differences ($\Delta C_d^{Core} = C_{d,ROM}^{Core}$ - C_d^{Core}) across the idle descent range considered was $\simeq 0.034$, with a confidence interval ($\sigma/\sqrt{N}$) of $\simeq 5.4 \times 10^{-3}$, where N is the number of samples considered. An independent test performed for flight condition M_0 for values of $FNPR_p \lesssim \lambda_{crit}$ (Fig. 4(b)) resulted in $\sigma_{\Delta C_d^{Core}} \simeq 0.0165$ based on six data points.

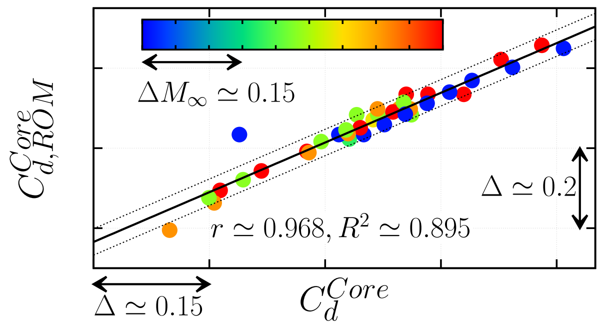

Figure 20: Variation of the estimated discharge coefficient from the ROM - ($C_{d,ROM}^{Core}$) with the computed discharge coefficient values (C_d^{Core}) obtained from the simulations for the installed cases. The solid black line is the regression line with a slope of $\simeq 39.5°$, and the dotted lines denote one standard deviation of ΔC_d^{Core}. The points are coloured by M_∞.

A ROM to predict C_d^{Core} can be developed with a limited CFD dataset by relating the core mass flow to the effective core nozzle pressure ratio (Eq. 9). Thus, for an installed engine, the static pressure at the base of the core nozzle is an indicative measure of the effective core nozzle pressure ratio. This has been utilised to derive a ROM to obtain reasonable estimates of C_d^{Core} for a HBR engine across a wide range of off-design operating conditions. The developed ROM can be used in 0D engine performance analysis methods to predict the impact of installation on engine performance in terms of turbomachinery re-matching and shaft-speed variations across the idle descent range.

4. Conclusions

The exhaust nozzle performance of an aero-engine has been investigated at idle descent conditions for different levels of engine integration. The impact of the installation of an aero-engine plays a significant role in determining the discharge coefficients of the bypass and core nozzles, with several competing flow mechanisms governing the nozzle mass flow rates. The maximum difference in C_d^{Bypass} between the installed and isolated engines is $\simeq 1.6\%$ across the descent phase. The impact of installation on C_d^{Core} is significant, with the difference between the installed and isolated engine with the pylon ranging between $\simeq 43\%$ at the top of descent to $\simeq -5.4\%$ at the end of descent. A combination of flow mechanisms such as engine-airframe interaction, wing loading, and the bypass nozzle pressure ratio influence the static pressure on the core cowl after-body, which leads the core nozzle to discharge to a pressure field different from the ambient static pressure. These effects need to be considered from a performance modelling perspective, as it influences the core nozzle mass flow, and subsequently, the operating point of the upstream engine components. A correlation can be derived by relating the mass flow from the core nozzle to an effective core nozzle pressure ratio based on the mean static pressure at the base of the core nozzle exit. This correlation has been utilised to develop a ROM to provide good estimates of C_d^{Core} for the installed HBR engine at idle descent conditions. It was shown that it is feasible to develop a reduced order model to estimate the large changes in core nozzle discharge coefficient due to engine installation under descent conditions.

Conflict of Interest

The author(s) declare no potential conflicts of interest with respect to the research, authorship, and/or publication of this article.

Data statement

Due to commercial confidentiality agreements, the supporting data is not available.

Acknowledgements

The authors would like to acknowledge the financial support from the European Commission Clean Sky 2 project grant agreement number 785349—H2020-CS2-CFP06-2017-01 under the PROTEUS (PeRformance & Operability of Turbofan Engines Under Sub-idle) project. The authors would also like to acknowledge the computing facilities provided by Cranfield University, UK. Lastly, the authors would like to thank Dr. Alexander Heidebrecht for the fruitful technical discussions over the course of this project.

References

[1] Robinson, J. E. and Kamgarpour, M., "Benefits of Continuous Descent Operations in High-Density Terminal Airspace Considering Scheduling Constraints," 10^{th} AIAA Aviation Technology, Integration, and Operations (ATIO) Conference, No. AIAA 2010-9115, Fort Worth, Texas, USA, 2010, pp. 1–21.

[2] Cao, Y., Jin, L., Nguyen, N. V. P., Landry, S., Sun, D., and Post, J., "Evaluation of Fuel Benefits Depending on Continuous Descent Approach Procedures," *Air Traffic Control Quarterly*, Vol. 22, No. 3, 2014, pp. 251–275.

[3] Pradeep, P. and Wei, P., "Predictability, variability and operational feasibility aspect of CDA," 2017 IEEE Aerospace Conference, Big Sky, MT, USA, 2017, pp. 1–14.

[4] Seitz, A., *Advanced methods for propulsion system integration in aircraft conceptual design*, Ph.D. thesis, Technische Universität München, 2012.

[5] Walsh, P. P. and Fletcher, P., *Gas Turbine Performance, 2nd edition*, John Wiley & Sons, 2004.

[6] García Rosa, N., Dufour, G., Barènes, R., and Lavergne, G., "Experimental Analysis of the Global Performance and the Flow Through a High-Bypass Turbofan in Windmilling Conditions," *Journal of Turbomachinery*, Vol. 137, No. 5, May 2015, pp. 51001–1 – 51001–8.

[7] Grech, N., *Gas Turbine Sub-idle Performance Modelling: Groundstart Altitude Relight, and Windmilling*, Ph.D. thesis, Cranfield University, School of Engineering, Power and Propulsion, 2013.

[8] Chapman, J. W. and Guo, T.-H., "Extending the operational envelope of a turbofan engine simulation into the sub-idle region," AIAA Atmospheric Flight Mechanics Conference, No. AIAA–2016–1043, San Diego, California, USA, 2016, pp. 1–11.

[9] Farokhi, S., *Aircraft Engines – A Review*, chap. 1, John Wiley & Sons, Ltd, 2019, pp. 1–107.

[10] Goulos, I., Stańkowski, T., Otter, J., MacManus, D., Grech, N., and Sheaf, C., "Aerodynamic Design of Separate-Jet Exhausts for Future Civil Aero-engines—Part I: Parametric Geometry Definition and Computational Fluid Dynamics Approach," *Journal of Engineering for Gas Turbines and Power*, Vol. 138, No. 8, March 2016, pp. 081201–1 – 081201–14.

[11] Farokhi, S., *Aircraft Propulsion*, Aircraft propulsion, John Wiley & Sons, Ltd, 2009.

[12] Goulos, I., Otter, J., Stańkowski, T., MacManus, D., Grech, N., and Sheaf, C., "Design optimisation of separate-jet exhausts for the next generation

of civil aero-engines," *The Aeronautical Journal*, Vol. 122, No. 1256, 2018, pp. 1586–1605.

[13] Otter, J. J., Stańkowski, T., Robinson, M., and MacManus, D. G., "Installation aerodynamics of civil aero-engine exhaust systems," *Aerospace Science and Technology*, Vol. 89, 2019, pp. 345–355.

[14] Guha, A., "Optimum Fan Pressure Ratio for Bypass Engines with Separate or Mixed Exhaust Streams," *AIAA Journal of Propulsion and Power*, Vol. 17, (5), September-October 2001, pp. 1117–1122.

[15] Hoheisel, H., "Aerodynamic aspects of engine-aircraft integration of transport aircraft," *Aerospace Science and Technology*, Vol. 1, No. 7, 1997, pp. 475 – 487.

[16] Geyr, H. and Rossow, C., "A Correct Thrust Determination Method for Turbine Powered Simulators in Wind Tunnel Testing," 41^{st} AIAA/ASME/SAE/ASEE Joint Propulsion Conference & Exhibit, No. AIAA 2005-3707, Tucson, Arizona, USA, 2005, pp. 1–12.

[17] Pratt & Whitney, "PurePower Engine Family Specs Chart," `https://pdf.aeroexpo.online/pdf/pratt-whitney/pw1200g/170325-2447.html`, 2012, [Online; accessed 26-July-2021].

[18] Rolls Royce, "Trent 1000 infographic," `https://www.rolls-royce.com/~/media/Files/R/Rolls-Royce/documents/civil-aerospace-downloads/trent-1000-infographic.pdf`, 2016, [Online; accessed 26-July-2021].

[19] GE Aviation, "GE9X Commercial Aircraft Engine," `https://www.geaviation.com/commercial/engines/ge9x-commercial-aircraft-engine`, 2021, [Online; accessed 26-July-2021].

[20] Zheng, W., Wang, Y., Shan, J., Deng, X., and Tian, W., "Interference Effect of Engine Exhaust on Civil Aircraft Drag Performance," *Journal of Aircraft*, Vol. 49, December 2012, pp. 2001–2006.

[21] Stańkowski, T. P., MacManus, D. G., Sheaf, C. T. J., and Christie, R., "Aerodynamics of aero-engine installation," *Proceedings of the Institution of Mechanical Engineers, Part G: Journal of Aerospace Engineering*, Vol. 230, No. 14, 2016, pp. 2673–2692.

[22] Stańkowski, T. P., MacManus, D. G., Sheaf, C. T., and Grech, N., "Aerodynamics of Aero-Engine Installation," AIAA SciTech Forum, 54^{th} AIAA Aerospace

Sciences Meeting, 4-8 January 2016, No. AIAA 2016-0764, San Diego, USA, 2016, pp. 1–21.

[23] Stańkowski, T. P., MacManus, D. G., Robinson, M., and Sheaf, C. T., "Aerodynamic Effects of Propulsion Integration for High Bypass Ratio Engines," *Journal of Aircraft*, Vol. 54, No. 6, 2017, pp. 2270–2284.

[24] Burgsmüller, W. and Hoheisel, H., "ENIFAIR - EU research into engine integration on future transport aircraft," *Air and Space Europe*, Vol. 2, No. 2, 2000, pp. 81 – 85.

[25] Rossow, C.-C., Godard, J.-L., Hoheisel, H., and Schmitt, V., "Investigations of propulsion integration interference effects on a transport aircraft configuration," *Journal of Aircraft*, Vol. 31, No. 5, 1994, pp. 1022–1030.

[26] Goulos, I., Otter, J., Tejero, F., Rebassa, J. H., MacManus, D., and Sheaf, C., "Civil turbofan propulsion aerodynamics: Thrust-drag accounting and impact of engine installation position," *Aerospace Science and Technology*, Vol. 111, 2021, pp. 106533.

[27] Dusa, D., Lahti, D., and Berry, D., "Investigation of subsonic nacelle performance improvement concept," 18^{th} Joint Propulsion Conference, No. AIAA-82-1042, Cleveland, Ohio, USA, 1982, pp. 1–10.

[28] Harris, A. and Paliwal, K., "Civil turbofan propulsion system integration studies using powered testing techniques at ARA, Bedford," 13^{th} Aerodynamic Testing Conference, No. AIAA–84–0593, San Diego, California, USA, 1984, pp. 74–98.

[29] Li, J., Gao, Z., Huang, J., and Zhao, K., "Aerodynamic design optimization of nacelle/pylon position on an aircraft," *Chinese Journal of Aeronautics*, Vol. 26, No. 4, 2013, pp. 850 – 857.

[30] Oliveira, G., Trapp, L. G., and Puppin-Macedo, A., "Engine-Airframe Integration Methodology for Regional Jet Aircrafts with Underwing Engines," 41^{st} Aerospace Sciences Meeting and Exhibit, No. AIAA 2003-934, Reno, Nevada, USA, 2003, pp. 1–15.

[31] Tejero, F., Goulos, I., MacManus, D., and Sheaf, C., "Effects of Aircraft Integration on Compact Nacelle Aerodynamics," Proceedings of the 2020 AIAA Scitech 2020 Forum, 6-10 January, No. AIAA 2020-2225, Orlando, Florida, USA, 2020, pp. 1–19.

[32] Kim, S. H., Yee, K. J., and Oh, S. J., "Numerical Investigation Of Shock-buffet On Transport Aircraft With Changing The Position Of Nacelle/pylon," *Journal of Computational Fluids Engineering*, Vol. 19, September 2014, pp. 69–76.

[33] Dietz, G., Mai, H., Schröder, A., Klein, C., Moreaux, N., and Leconte, P., "Unsteady Wing-Pylon-Nacelle Interference in Transonic Flow," *Journal of Aircraft*, Vol. 45, No. 3, 2008, pp. 934–944.

[34] Berry, D. L., "The Boeing 777 Engine/Airframe Integration Aerodynamic Design Process," Proceedings of the 19^{th} Congress of the International Council of Aerospace Science, Vol. ICAS-94-6.4.4, Anaheim, California, USA, 1994, pp. 1305–1305.

[35] Rudnik, R., Rossow, C.-C., and Geyr, H. F. v., "Numerical simulation of engine/airframe integration for high-bypass engines," *Aerospace Science and Technology*, Vol. 6, No. 1, 2002, pp. 31 – 42.

[36] Obert, E., *Aerodynamic Design of Transport Aircraft*, IOS Press BV, Amsterdam, 2009.

[37] Otter, J. J., Goulos, I., MacManus, D. G., and Slaby, M., "Aerodynamic Analysis of Civil Aeroengine Exhaust Systems Using Computational Fluid Dynamics," *Journal of Propulsion and Power*, Vol. 34, No. 5, 2018, pp. 1152–1165.

[38] Otter, J. J., Goulos, I., Christie, R., and MacManus, D. G., "Design and analysis of non-axisymmetric installed aero-engine exhaust systems," *Aerospace Science and Technology*, Vol. 106, 2020, pp. 106210.

[39] EASA, "Certification Memorandum: Turbine Engine Relighting in Flight," European Aviation Safety Agency, Report EASA CM No.: CM-PIFS-010 01, 2015.

[40] Zachos, P. K., "Modelling and Analysis of Turbofan Engines Under Windmilling Conditions," *Journal of Propulsion and Power*, Vol. 29, No. 4, 2013, pp. 882–890.

[41] Ferrer-Vidal, L. E., Iglesias-Pérez, A., and Pachidis, V., "Characterization of axial compressor performance at locked rotor and torque-free windmill conditions," *Aerospace Science and Technology*, Vol. 101, 2020, pp. 105846.

[42] Goulos, I., Otter, J., Stańkowski, T., MacManus, D., Grech, N., and Sheaf, C., "Aerodynamic Design of Separate-Jet Exhausts for Future Civil Aero-engines—Part II: Design Space Exploration, Surrogate Modeling, and Opti-

mization," *Journal of Engineering for Gas Turbines and Power*, Vol. 138, No. 8, March 2016, pp. 081202–1 – 081202–14.

[43] Goulos, I., Stańkowski, T., MacManus, D., Woodrow, P., and Sheaf, C., "Civil turbofan engine exhaust aerodynamics: Impact of bypass nozzle after-body design," *Aerospace Science and Technology*, Vol. 73, 2018, pp. 85 – 95.

[44] Goulos, I., MacManus, D., and Sheaf, C., "Civil turbofan engine exhaust aerodynamics: Impact of fan exit flow characteristics," *Aerospace Science and Technology*, Vol. 93, 2019, pp. 105181.

[45] Zhang, Y., Chen, H., Zhang, M., Zhang, M., Li, Z., and Fu, S., "Performance Prediction of Conical Nozzle Using Navier–Stokes Computation," *Journal of Propulsion and Power*, Vol. 31, No. 1, 2015, pp. 192–203.

[46] Zhang, Y., Chen, H., Fu, S., Zhang, M., and Zhang, M., "Drag prediction method of powered-on civil aircraft based on thrust drag bookkeeping," *Chinese Journal of Aeronautics*, Vol. 28, No. 4, 2015, pp. 1023 – 1033.

[47] Zhu, F. and Qin, N., "Intuitive Class/Shape Function Parameterization for Airfoils," *AIAA Journal*, Vol. 52, No. 1, 2014, pp. 17–25.

[48] Otter, J. J., Christie, R., Goulos, I., MacManus, D. G., and Grech, N., "Parametric design of non-axisymmetric separate–jet aero-engine exhaust systems," *Aerospace Science and Technology*, Vol. 93, 2019, pp. 105186.

[49] Tejero, F., Robinson, M., MacManus, D. G., and Sheaf, C., "Multi-objective optimisation of short nacelles for high bypass ratio engines," *Aerospace Science and Technology*, Vol. 91, 2019, pp. 410–421.

[50] Lee, Y.-S., Ma, Y., and Jegadesh, G., "Rolling-ball method and contour marching approach to identifying critical regions for complex surface machining," *Computers in Industry*, Vol. 41, No. 2, 2000, pp. 163 – 180.

[51] Vassberg, J. C., Dehaan, M. A., Rivers, M. B., and Wahls, R. A., "Development of a Common Research Model for Applied CFD Validation Studies," 26^{th} AIAA Applied Aerodynamics Conference, No. AIAA 2008-6919, Honolulu, Hawaii, USA, 2008, pp. 1–22.

[52] Rivers, M. and Dittberner, A., "Experimental Investigations of the NASA Common Research Model in the NASA Langley National Transonic Facility and NASA Ames 11-Ft Transonic Wind Tunnel," 49^{th} AIAA Aerospace Sciences

Meeting including the New Horizons Forum and Aerospace Exposition, No. AIAA 2011-1126, Orlando, Florida, USA, June 2011, pp. 1–28.

[53] Vassberg, J. C., Tinoco, E. N., Mani, M., and Rider, B., "Summary of the Fourth AIAA CFD Drag Prediction Workshop," 29^{th} AIAA Applied Aerodynamics Conference, No. AIAA 2010-4547, Chicago, Illinois, USA, 2010, pp. 1 – 29.

[54] Brodersen, O., "Computation of Engine-Airframe Installation Drag," MEGAFLOW - Numerical Flow Simulation for Aircraft Design, edited by N. Kroll and J. K. Fassbender, Springer Berlin Heidelberg, Germany, 2005, pp. 151–161.

[55] Ansys, I., *ANSYS Meshing Theory Guide: Release 18.2*, 2017.

[56] Celik, I. B., Ghia, U., Roache, P. J., Freitas, C. J., Coleman, H., and Raad, P. E., "Procedure for Estimation and Reporting of Uncertainty Due to Discretization in CFD Applications," *Journal of Fluids Engineering*, Vol. 130, July 2008, pp. 078001–1 – 078001–4.

[57] Weiss, J., Maruszewski, J., Smith, W., Smith, W., Weiss, J., and Maruszewski, J., "Implicit solution of the Navier–Stokes equations on unstructured meshes," 13^{th} Computational Fluid Dynamics Conference, No. AIAA-97-2103, Snowmass Village, Colorado, USA, 1997, pp. 139–149.

[58] Menter, F. R., "Two-equation eddy-viscosity turbulence models for engineering applications," *AIAA Journal*, Vol. 32, No. 8, 1994, pp. 1598–1605.

[59] Ansys, I., *ANSYS FLUENT Theory Guide: Release 18.2*, 2017.

[60] Sutherland, W., "The viscosity of gases and molecular force," *The London, Edinburgh, and Dublin Philosophical Magazine and Journal of Science*, Vol. 36, No. 223, 1893, pp. 507–531.

[61] Giangaspero, G., MacManus, D., and Goulos, I., "Surrogate models for the prediction of the aerodynamic performance of exhaust systems," *Aerospace Science and Technology*, Vol. 92, 2019, pp. 77 – 90.

[62] Levy, D., Laflin, K. R., Tinoco, E. N., Vassberg, J. C., Mani, M., Rider, B., Rumsey, C., Wahls, R. A., Morisson, J. H., Brodersen, O. P., Crippa, S., Mavriplis, D., and Murayama, M., "Summary of Data from the Fifth AIAA

CFD Drag Prediction Workshop," 51^{st} AIAA Aerospace Sciences Meeting Including the New Horizons Forum and Aerospace Exposition, No. AIAA 2013-0046, Grapevine (Dallas/Ft. Worth Region), Texas, USA, 2013, pp. 1–31.

[63] Mikkelsen, K. L., Myren, D. J., Dahl, D. G., and Christiansen, M., "Initial Subscale Performance Measurements of the AIAA Dual Separate Flow Reference (DSFR) Nozzle," 51^{st} AIAA/SAE/ASEE Joint Propulsion Conference, No. AIAA 2015-3883, Orlando, Florida, USA, 2015, pp. 1–30.

[64] Mihaescu, M., Semlitsch, B., Fuchs, L., and Gutmark, E. J., "Airframe Installation Effects on the Jet Exhausting a Coaxial Nozzle System of a Gas Turbine Engine," Volume 1: Aircraft Engine; Ceramics; Coal, Biomass and Alternative Fuels; Controls, Diagnostics and Instrumentation, No. GT2012-69631 in Turbo Expo: Power for Land, Sea, and Air, June 2012, pp. 347–355.

[65] Del Mônaco Monteiro, P., Machiaverni, R. M., Bringhenti, C., and Tomita, J. T., "In-flight thrust determination for high-bypass-ratio turbofan using residual error methodology," *Journal of the Brazilian Society of Mechanical Sciences and Engineering*, Vol. 40, No. 2, January 2018, pp. 74.

[66] Hunt, D., "Experimental techniques used to evaluate propulsion system interference effects on the cruise configuration of the Boeing C-14," 17^{th} Aerospace Sciences Meeting, No. AIAA 1979-0035, New Orleans, LA, USA, 1979, pp. 1–10.

[67] Mikkelsen, K. L., McDonald, T., and Saiyed, N., "Static and Wind Tunnel Aero-Performance Tests of NASA AST Separate Flow Nozzle Noise Reduction Configurations," National Aeronautics and Space Administration- Glenn Research Center, NASA/CR-2001-210712, E-12658, NAS 1.26:210712, March 2001.

[68] Claus, R. W., Evans, A. L., Lylte, J. K., and Nichols, L. D., "Numerical Propulsion System Simulation," *Computing Systems in Engineering*, Vol. 2, No. 4, 1991, pp. 357 – 364.

2021-09-20

Impact of installation on a civil large turbofan exhaust system at idle descent conditions

Rao, Anirudh Narayan

Elsevier

Rao AN, Goulos I, MacManus DG. (2021) Impact of installation on a civil large turbofan exhaust system at idle descent conditions. Aerospace Science and Technology, Volume 119, December 2021, Article number 107125

https://doi.org/10.1016/j.ast.2021.107125